*American Mineralogist, Volume 107, pages 1133–1148, 2022*

# In situ chemical and isotopic analyses and element mapping of multiple-generation pyrite: Evidence of episodic gold mobilization and deposition for the Qiucun epithermal gold deposit in Southeast China

**Ying Ma[1,2], Shao-Yong Jiang[1,*], Hartwig E. Frimmel[2,3], and Lü-Yun Zhu[1,4]**

[1]State Key Laboratory of Geological Processes and Mineral Resources, School of Earth Resources, Collaborative Innovation Center for Exploration of Strategic Mineral Resources, China University of Geosciences, Wuhan 430074, P.R. China
[2]Bavarian Georesources Center, Institute of Geography and Geology, University of Würzburg, Am Hubland, Würzburg 97074, Germany
[3]Department of Geological Sciences, University of Cape Town, Rondebosch 7700, South Africa
[4]College of Zijin Mining, Fuzhou University, Fuzhou 350108, P.R. China

## Abstract

Gold deposits are often the result of complex mineralization and remobilization processes. Interpretation of bulk geochemical and sulfur isotope data of the gold deposits is frequently hampered by complex zoning in pyrite, which calls for in situ determination of geochemical and sulfur isotope composition of sulfide minerals. The Qiucun deposit is a good representative of epithermal gold deposits in the Mesozoic Coastal Volcanic Belt of southeastern China. It represents a complex mineralization history, comprising three hydrothermal stages: (I) early stage of pyrite-quartz-chalcedony; (II) main ore stage of quartz-polymetallic sulfide; and (III) post-ore stage of quartz-carbonate. Detailed backscattered electron imaging (BSE) and in situ trace element and sulfur isotope analyses using laser ablation-inductively coupled plasma-mass spectrometry (LA-ICP-MS) and LA-multicollector (MC)-ICP-MS were applied to reveal the gold mineralization and remobilization history of this deposit. Four texturally distinct generations of pyrite were identified, all of which host invisible gold: $Py_{1a}$ and $Py_{1b}$ in Stage I and $Py_{2a}$ and $Py_{2b}$ in Stage II. A detailed study of the texture, chemistry, and sulfur isotopic composition as well as hydrothermal evolution of auriferous pyrite from the Qiucun deposit revealed the behavior of gold in the course of pyrite evolution. Pyrite of Stages I and II contains invisible gold, whereas later-stage visible native gold and re-enrichment in invisible gold is associated with alteration rims around the primary pyrite grains. $Py_{1a}$ is rich in silicate inclusions, enriched in Co and Ni, and depleted in As and Au relative to later pyrite generations. This redistribution is attributed to the alteration of biotite in the sub-volcanic host rocks that effectively destabilized gold in the ore fluid during $Py_{1a}$ deposition. $Py_{1b}$ and $Py_{2a}$ show oscillatory zoning with bright bands having elevated As and Au contents. The oscillatory zoning is interpreted to reflect pressure fluctuations and repeated local fluid boiling around the pyrite crystals. These three pyrite generations ($Py_{1a}$, $Py_{1b}$, $Py_{2a}$) record a narrow range of $\delta^{34}S_{V\text{-}CDT}$ values between –3.6 and 4.6‰, consistent with a magmatic sulfur source. Gold and some trace elements (As, Ag, Sb, Pb, Tl, and Cu) that were initially incorporated into $Py_{2a}$ became partially exsolved and remobilized during the replacement of porous and invisible gold-rich $Py_{2b}$. This replacement was likely due to coupled dissolution and re-precipitation reactions triggered by oxidation of the mineralizing fluids. Fluid oxidation is further supported by a general decrease trend of $\delta^{34}S_{V\text{-}CDT}$ from $Py_{2a}$ (–3.2 to 4.6‰) to $Py_{2b}$ (–15.2 to –2.3‰). Last, previously formed auriferous pyrite underwent post-mineralization fracturing, causing local pulverization of pyrite. Thus, newly created porosity facilitated fluid circulation, hydrothermal alteration of the pyrite, and remobilization of invisible gold, which re-precipitated with pyrite in the form of electrum as small inclusions or as larger grains within fractures. Our study emphasizes that pressure-driven hydrothermal processes play a vital role in the initial enrichment and re-concentration of gold and some other trace metals during episodic deposition, replacement, and hydrothermal alteration of gold-bearing pyrite in epithermal gold deposits, ultimately forming visible gold and high-grade ore shoots as exemplified by the Qiucun deposit.

**Keywords:** Pyrite formation and replacement, sulfur isotopes, gold remobilization, epithermal gold mineralization

## Introduction

Large gold deposits may form by multiple gold enrichment events, but it is often hard to clarify whether the last of these events represents remobilized gold from pre-existing mineralization or relates to new gold introduction during a distinct epigenetic event (Large et al. 2009; Haroldson et al. 2018). In many gold deposits, gold shows a bimodal distribution in which refractory gold within pyrite was overprinted by later visible gold as distinct inclusions or filling fractures within the pyrite. The former is either primary in origin or a result of the remobilization of refractory gold. In contrast, the latter is considered to be remobilized invisible gold within fractures of the pyrite (e.g., Morey et al. 2008; Cook et al. 2009; Large et al. 2011). This gold remobilization could lead to secondary gold enrichment and help understand the origin of bonanza zones within gold deposits, which considerably enhance bulk gold grade.

* E-mail: shyjiang@cug.edu.cn. Orcid 0000-0003-3921-739X

0003-004X/22/0006–1133$05.00/DOI: https://doi.org/10.2138/am-2022-8030

Pyrite occurs in various crustal environments and is one of the most important host minerals for gold. Gold incorporated in pyrite as solid solution ($Au^{+}$) and/or submicrometer particles ($Au^{0}$) is referred to as invisible (refractory) gold (Gopon et al. 2019). This type of gold, which can reach concentrations from tens of ppb to >1 wt% (Deditius et al. 2014), is generally thought to be a primary precipitation feature (e.g., Reich et al. 2005; Velásquez et al. 2014). However, the physicochemical controls on this type of gold mineralization are still under debate, with fluid temperature, pH, oxidation state, and sulfur fugacity all playing potentially important roles (Gregory et al. 2019).

The texture and chemistry of pyrite have been used extensively in unraveling the genesis and evolution of many ore deposits (Franchini et al. 2015; Sykora et al. 2018). The texture and morphology of pyrite can reflect replacement or dissolution and can also be used to distinguish between supersaturation, near-equilibrium crystallization, or recrystallization. The trace element distribution in pyrite and included nanoparticles may reveal changes in temperature, pH, oxidation state, source, and composition of the ore fluid (e.g., Deditius et al. 2011; Velásquez et al. 2014). The sulfur isotope ratios of pyrite can provide useful information on the fluid source and decipher physicochemical conditions during precipitation (Ohmoto 1972). However, interpretation of geochemical and sulfur isotope data is far from straightforward because gold-bearing pyrite usually results from multiple stages of overgrowths. Thus, geochemical and sulfur isotope data derived using bulk analysis represent a mixed signal, from which no definite conclusion can be drawn. In situ determination of trace element concentrations, in combination with sulfur isotope analysis, has been used more and more in the past few years, and the high spatial resolution of these techniques provides a promising tool to reveal complex overgrowths in single grains and to reveal the detailed episodic gold deposition and remobilization history in gold deposits (Morey et al. 2008; Cook et al. 2009; Velásquez et al. 2014; Gregory et al. 2019).

The Mesozoic Coastal Volcanic Belt in southeastern China is one of the most important mineral provinces in China, hosting many epithermal gold deposits, with a total gold reserve of over 480 t, including the world-class Zijinshan gold deposit [323 t Au, average grade: 0.5 g/t (Zhong et al. 2017; White et al. 2019)]. This contribution reports on the mineralogical distribution of gold in the Qiucun epithermal deposit in the Dehua goldfield of southeastern China (Fig. 1). There, gold occurs as both visible gold and as Au-rich pyritic refractory ore. A fluid inclusion study by Ni et al. (2018) suggested that mineralization took place at 180−250 °C, and the ore fluid was dilute (<2.6 wt% NaCl equiv.), near-neutral, $CO_2$-bearing, and formed during boiling. Liu (2018) proposed that the mineralizing fluid consisted of a mixture of magmatic and meteoric components based on stable isotope data. Despite the many studies on the mine geology, fluid inclusions, and stable isotopes, the mineralogy and mineral paragenesis of this deposit remains poorly understood.

Previous studies showed that the auriferous pyrite in the Dehua goldfield is commonly zoned (Zhang et al. 2018) in its chemical and S isotopic composition. Consequently, traditional whole-grain analyses must be considered as "average compositions" of different zones. The situation is even further complicated by minute mineral inclusions in the pyrite. In this study, we used in situ LA-ICP-MS trace element spot and map analyses to investigate the textural and crystal-chemical relationships between gold and the associated metals in the hosting pyrite. A link between multi-stage pyrite formation and initial gold deposition is established, and the effect of pyrite deformation on the remobilization of gold in the epithermal environment is described. Last, we conducted in situ LA-MC-ICP-MS sulfur isotope analysis of texturally complex pyrite to examine microscopic variations of sulfur isotope compositions in the ore-forming processes. The results are used to track the sulfur source and the changes in the physicochemical conditions during ore formation.

## Geological background

### Regional geology

The South China Block (SCB) resulted from the amalgamation of the Cathaysia and Yangtze blocks during Neoproterozoic times (Fig. 1a; Wang and Li 2003). After two intraplate orogenies during the Early Paleozoic and Early Mesozoic (Shu et al. 2015), a western Pacific continental margin formed in the SCB in the Late Mesozoic, marking a change from Tethyan to Pacific tectonism (Zhou et al. 2006). Since the Early Jurassic, the westward subduction of the paleo-Pacific plate beneath the SCB has induced large-scale lithospheric extension and intensive magmatism, which produced the Mesozoic Coastal Volcanic Belt in the southeastern margin of the SCB (Fig. 1b; Zhou et al. 2006).

The Dehua goldfield represents a typical example of mineralization within the Coastal Volcanic Belt (Fig. 1b; Ma et al. 2021a). Neoproterozoic metamorphic basement, Paleozoic to Triassic clastic sedimentary rocks, and Jurassic continental clastic and volcanic rocks are the major rock types in the area (Fig. 2a). The Jurassic strata of the Dehua area are subdivided, in ascending order, into the Lishan Formation sandstone, the Changlin Formation sandstone, and the comparatively widespread Nanyuan Formation (Fig. 2a). The latter is composed of Late Jurassic, 169−157 Ma dacitic to rhyolitic tuff, rhyolite, and tuffaceous sandstone (Li et al. 2020). These volcano-sedimentary rocks host the epithermal gold deposits (e.g., Dongyang, Qiucun, Ancun, Lingtouping, and Chunhu) in the region (Fig. 2b).

The sedimentary units of the Dehua area were intruded by widespread Silurian and subordinate Triassic and Jurassic to Cretaceous granitic magmas (Fig. 2a), which were generated by partial melting of the Proterozoic basement rocks (Shu et al. 2015). The main geologic structures of the Dehua goldfield include a series of northeast (NE), northwest (NW), and nearly north-south (N-S) striking faults (Fig. 2a). The NE- and NW-striking faults of Mesozoic age are two sets of the most important structures, spatially controlling the emplacement of Mesozoic granites and the distribution of gold deposits (Fig. 2a).

### Geology of the Qiucun gold deposit

The Qiucun deposit is situated in the northern portion of the Dehua goldfield (Fig. 2a). It is hosted mainly by sub-volcanic rocks of the Nanyuan Formation, subordinately by sandstone of the Changlin Formation (Figs. 2b–2c). The exposed intrusive rocks are mainly Silurian quartz diorite, Jurassic rhyolite porphyry and diorite dikes (Figs. 2b–2c). The major structures in the Qiucun area are NW-striking normal and NE-striking reverse

faults (Fig. 2b). The latter is represented by the $F_1$, $F_2$, $F_3$, $F_7$, $F_{11}$, $F_{12}$, and $F_{13}$ (Fig. 2b), which are largely filled by quartz veins (in places auriferous) and diorite dikes, striking 45–60° and dipping 45–89° to the southeast (Figs. 2b–2c; Fan 2015). The NW-striking normal faults are younger than the mineralization (locally referred to as the $F_{19}$, $F_{20}$, $F_{301}$; Fig. 2b) and located in the northeastern and southeastern parts of the deposit.

The Qiucun gold deposit consisted of 16 orebodies with a total proven reserve of 10 t Au in 2017 (Huang et al. 2017). The largest gold orebody, named $Au_{11}$, extends from 940 to 660 m in elevation, dips to the northwest at 70°, and varies in thickness from 0.6 to 34 m (average 4.0 m), with a Au grade of 4.9 g/t and a strike length of about 310 m (Fig. 2c). Gold is present in economic concentrations (3 to 30 g/t) and is largely confined to quartz veins and silicified hydrothermal breccias and wall rocks. Wall rock alteration is pervasive and is best developed adjacent to the auriferous quartz veins and breccias. The alteration assemblages consist mainly of quartz, sericite, chlorite, illite, and carbonate, with minor disseminations of pyrite. Higher gold concentrations (locally reaching bonanza grades of 300–500 g/t) predominate at depth in a zone of postulated high fluid flow rate, repeated hydraulic fracturing, and episodic boiling.

## Sampling and analytical methods

### Electron microprobe analysis

Eleven hand-specimen samples (Online Materials[1] Table A1), representative of mineralization Stages I and II, were collected from underground at the 712, 742, and 802 m levels. Polished thin sections containing sufficient amounts of sulfide minerals and their host rocks were characterized by electron microprobe analysis (EMPA). The EMPA was performed using a JEOL JXA-8230 superprobe housed at the Testing Center of the China Metallurgical Geological Bureau, Shandong. Standards and unknowns were analyzed using a 5 μm beam diameter, an accelerating voltage of 20 kV, and a beam current of 20 nA. Calibration standards used were pyrite for S and Fe, chalcopyrite for Cu, sphalerite for Zn, galena for Pb, and alloy or pure metal for As, Co, Ni, Sb, Ag, and Au. The detection limits for each element were as follows: S (109 ppm), Fe (149 ppm), As (234 ppm), Co (80 ppm), Ni (93 ppm), Sb (361 ppm), Pb (438 ppm), Cu (227 ppm), Au (818 ppm), Ag (272 ppm), and Zn (299 ppm). The data were reduced using the ZAF correction method.

### In situ trace element analysis of pyrite

Trace element concentrations of pyrite were conducted using LA-ICP-MS housed at the Nanjing FocuMs Technology Co. Ltd., China. The analytical instrumentation employed in this study was a Photon Machines Analyte G2 193 nm ArF excimer laser ablation system attached to an Agilent 7700x Quadrupole ICP-MS. The operating conditions and procedures applied to pyrite have been detailed in Gao et al. (2015). Spot analyses were used for individual analyses of various chemical zones as determined by EMPA. Spot ablation was carried out using a spot size of 40 μm at 3.5 J/cm$^2$ and a 6 Hz repetition rate. Each analysis

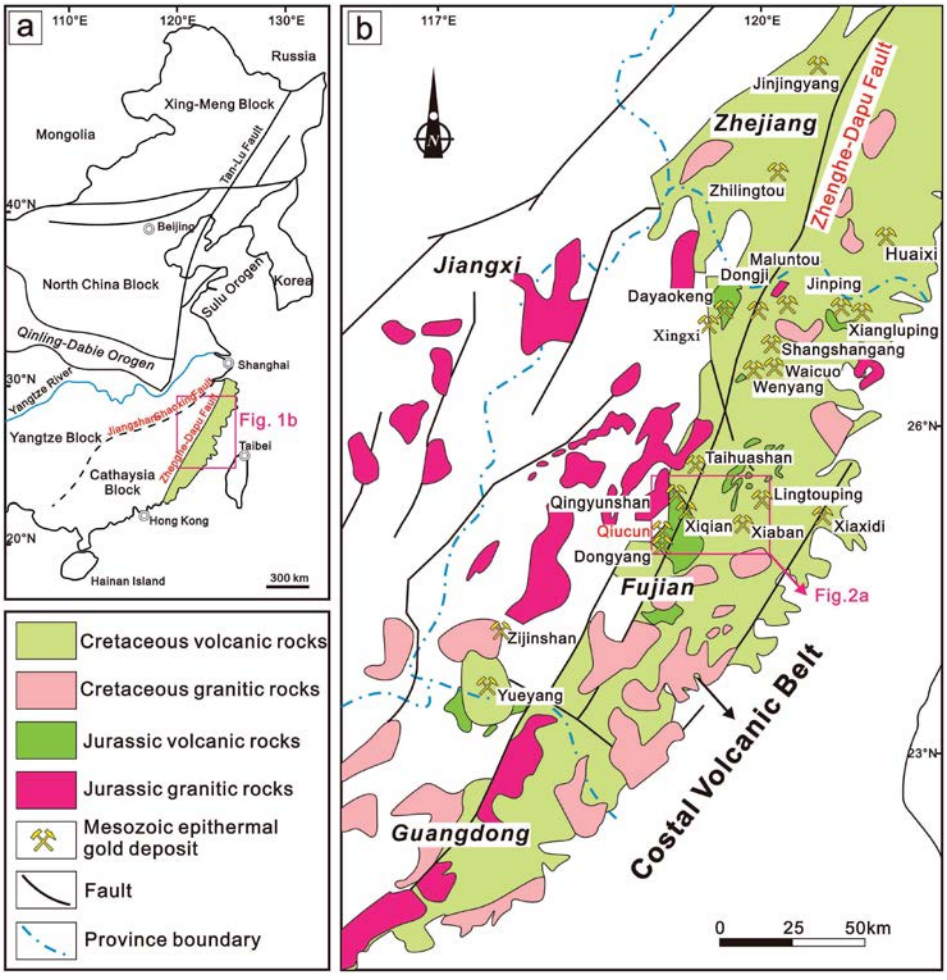


**Figure 1.** (**a**) Simplified map of the tectonic units of eastern China (Wu et al. 2005); (**b**) geologic map of the Coastal Volcanic Belt in southeastern China showing major faults, Late Mesozoic igneous rocks, and epithermal gold deposits (modified from Zhong et al. 2017).

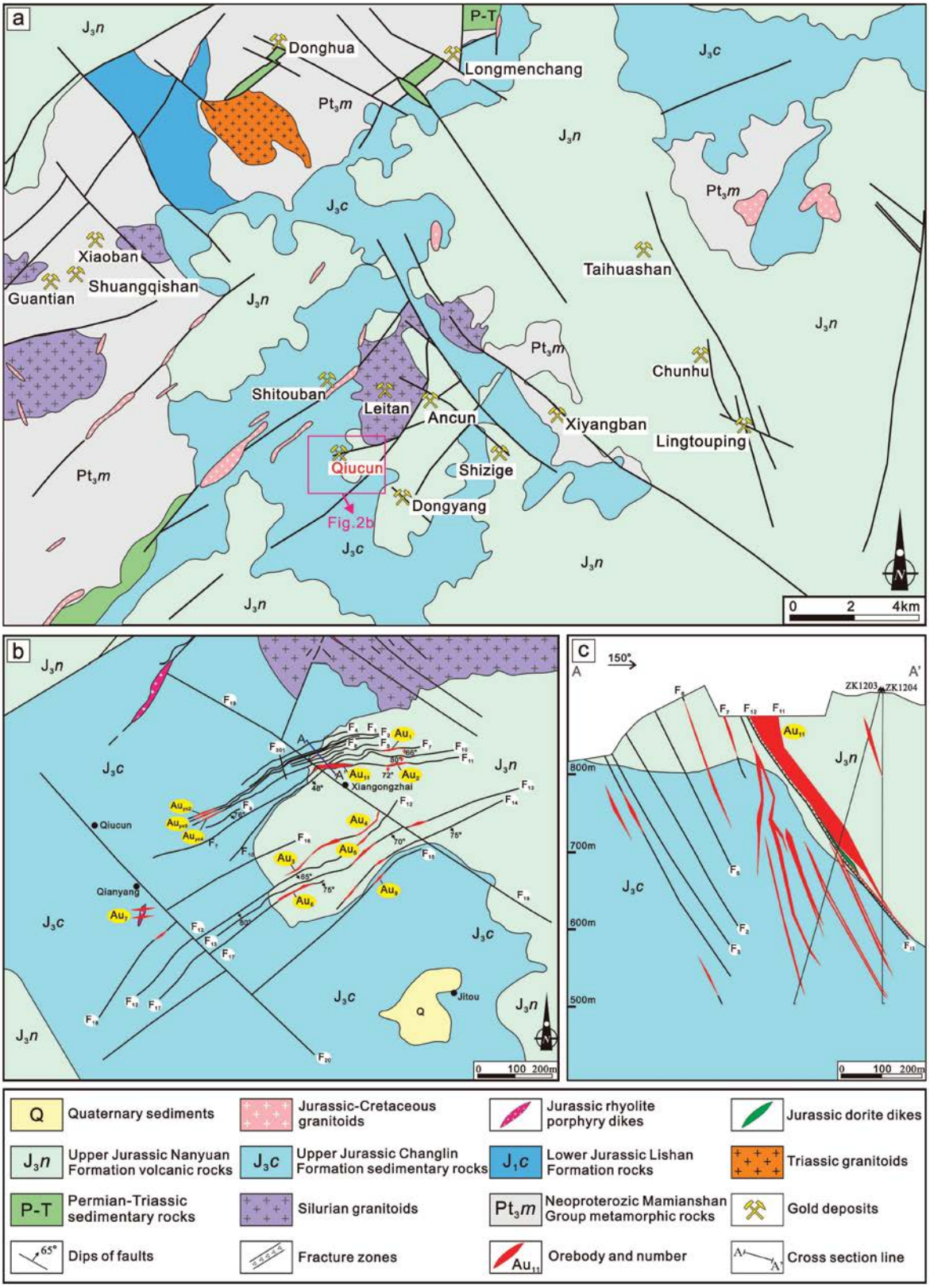


**Figure 2.** (**a**) Regional geologic map of the Dehua area showing the distribution of the gold deposits (modified from Jiang 2015); geologic map (**b**) and representative cross-section (**c**) of the Qiucun deposit, showing distribution and morphology of the gold orebodies (after Huang et al. 2017).

consisted of a 20 s laser-off period to measure background and a 35 s laser-on period for the analysis. USGS polymetallic sulfide pressed pellet MASS-1 and synthetic basaltic glasses GSE-1G were used for calibration (Wilson et al. 2002). Standard blocks were run after every ten unknown samples. Data reduction was performed offline using ICPDATACAL software (Liu et al. 2008), and the Fe content as determined by EMPA was used as a reference for the calculation of trace element concentrations.

### Element mapping of pyrite

Quantitative element distribution maps of pyrite grains were generated by LA-ICP-MS in the In Situ Mineral Geochemistry Lab at the Hefei University of Technology, China. Maps were acquired using a Photon Machines Analyte HE 193 nm laser ablation microprobe coupled to an Agilent 7900 Quadrupole ICP-MS. The maps were collected by rastering the laser over the region of interest with 45 s of washout between individual lines. Maps were acquired using a beam diameter of 15 µm with a laser repetition rate of 7 Hz and a scan velocity of 12 µm/s. The raw data were quantified and compiled into maps using the LIMS software package (Wang et al. 2017), with synthetic NIST SRM 610 glass as an external reference material, Fe as an internal reference, and BHVO-2G glass as a monitor for quality control (Jochum et al. 2005; Gourcerol et al. 2018; Kerr et al. 2018; Hastie et al. 2020). Considering the differences in ablation between silicate glasses (NIST 610) and sulfides, it is expected that fractionation limits the accuracy of the quantified data to ~20% (Wohlgemuth-Ueberwasser and Jochum 2015).

### In situ sulfur isotope analysis

Polished thin sections analyzed by LA-ICP-MS for trace element spot analysis were repolished and used for in situ sulfur isotope analysis. In situ S isotope analyses of pyrite were performed using a Nu Plasma II MC-ICP-MS together with a Resonetics-S155 193 nm laser ablation system housed at the GPMR, China University of Geosciences, Wuhan. The analytical methods and operating procedures followed the protocols described by Zhu et al. (2016). The diameter of the laser beam was 33 µm with a repetition rate of 8 Hz and an energy fluency of 3 J/cm$^2$. An in-house pyrite standard named WS-1 ($\delta^{34}S_{VCDT}$ = 1.1‰; Zhu et al. 2016) was used to correct the instrumental mass bias. The analytical precision is about 0.1‰.

## Results

### Mineralization stages and multiple generations of pyrite

Three mineralization stages are recognized based on field and petrographic observations (Figs. 3–6). Low-grade Stage I takes the form of fine- to medium-grained gray quartz-chalcedony with minor colloform and vuggy textures (Figs. 3a–3c). This stage also includes intergrowth of euhedral or subhedral pyrite. These veins were generally altered and overprinted by later hydrothermal fluids. Stage II is marked by fine-grained white to colorless quartz, and abundant aggregates, massive, or isolated crystals of sulfide minerals (Figs. 3d–3e). The ore minerals include pyrite, sphalerite, chalcopyrite, galena, and electrum. Calcite and lesser amounts of quartz characterize the Stage III (Fig. 3f).

Pyrite is the predominant sulfide mineral in both Stage I and II veins. Petrographic observations and BSE imaging revealed four generations of pyrite (Fig. 5). The data set of major element concentrations in pyrite is given in Online Materials[1] Table A2. Pyrite ($Py_1$) from Stage I veins consists of two generations: inclusion-rich anhedral cores ($Py_{1a}$, Figs. 5a–5b), which show neither dissolution textures nor the presence of pores, followed by an inclusion-free outer part of a rhythmic alternation of As-rich (As = 1.0–5.7 wt%) and As-poor zones (As = 0.61–0.91 wt%) ($Py_{1b}$, Fig. 5b). Concentrations of As are relatively low (<0.45 wt%), and all Au contents are below the EMPA detection limit of 975 ppm. Mineral inclusions found in $Py_{1a}$ and rare inclusions in $Py_{1b}$ are mainly quartz, rutile, apatite, sericite, chalcopyrite, and galena.

Two distinct generations of pyrite ($Py_{2a}$ and $Py_{2b}$) are recognized in the Stage II veins. $Py_{2a}$, with rare or no silicate inclusions,

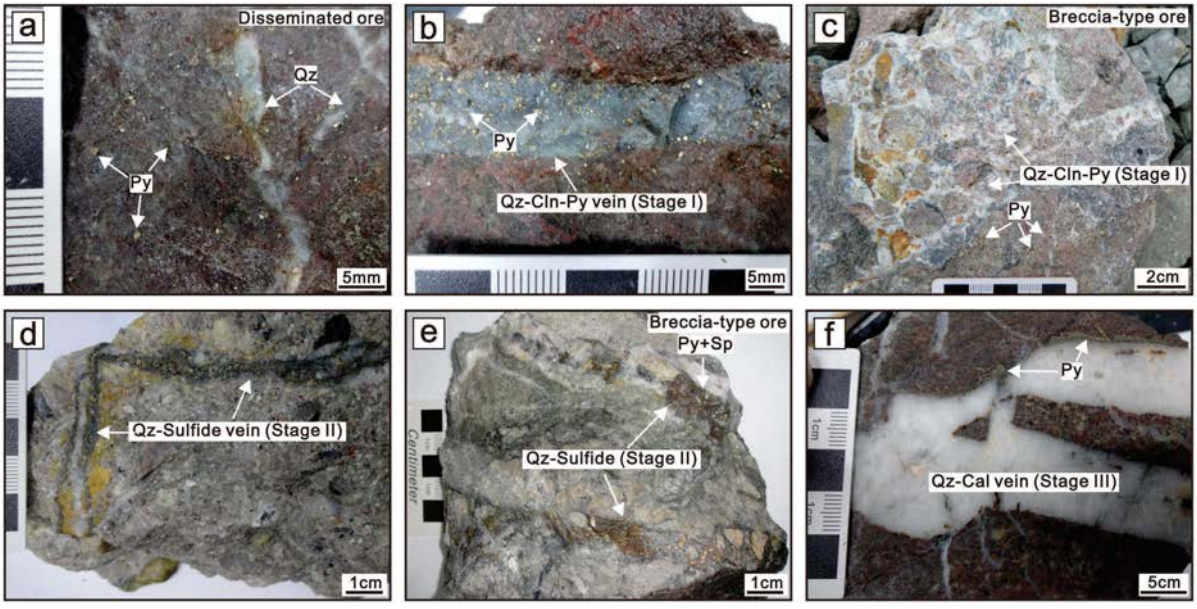


**Figure 3.** Photographs illustrating textures of gold ores of the Qiucun gold deposit. (**a**) Quartz veins crosscutting the disseminated pyrite ores. (**b**) Smoky-gray quartz-chalcedony-pyrite vein of Stage I within the volcanic rocks of the Nanyuan Formation. (**c**) Stage I veins showing the quartz-chalcedony-pyrite-cemented breccias of wall rocks. (**d**) Stage III quartz-sulfides veins crosscutting the sandstone of the Changlin Formation. (**e**) Quartz-sulfides cementing and cutting wall rocks breccias. (**f**) Stage III quartz-calcite vein with pyrite as anhedral aggregates near the vein margin. Abbreviations: Cal = calcite; Py = pyrite; Qz = quartz.

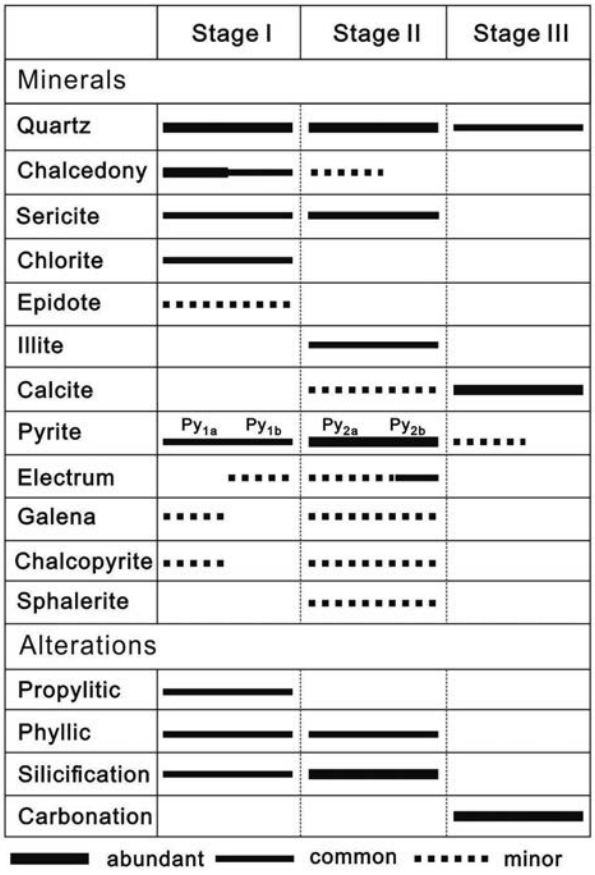


**Figure 4.** Paragenetic sequence of Qiucun gold mineralization interpreted from textures and pyrite geochemistry. Line thickness indicates approximate relative mineral abundance. Abbreviation: Py = pyrite.

commonly occurs as subhedral to anhedral overgrowth with oscillatory zoning around $Py_1$ (Figs. 5d–5e). It is coarse- (Figs. 5d–5e) to fine-grained (Fig. 5f) and its size ranges from 10 µm to 1 mm. The oscillatory zoning is made up of rhythmically alternating thin bright bands in BSE with high As (0.56–4.2 wt%) and broader, darker bands with low As (bdl–0.40 wt%) (Figs. 5d–5e). $Py_{2b}$ borders $Py_{2a}$ (Figs. 5g–5i) and is also present in microfractures of $Py_{2a}$ (Fig. 5g). $Py_{2b}$ is characterized by abundant pores of varying sizes (1–30 µm in diameter), which exhibit no perceptible preferred orientation. $Py_{2b}$ has high concentrations of As (1.3–4.8 wt%), causing a bright appearance in BSE images. The As-Fe-S ternary diagram (Fig. 7a) and the As vs. S plot of various pyrite generations (Fig. 7b) suggests that As is bound to the structure of pyrite in substitution for sulfur as $Fe(As_XS_{1-X})_2$, corresponding to the arsenian pyrite of the $As^{-1}$ type (Simon et al. 1999). This is confirmed by the flat $^{75}As$ spectrum in-depth profiles shown in Online Materials[1] Figure A1, which supports the notion of As being present as a solid solution.

### Trace element distribution in pyrite

A total of 112 LA-ICP-MS spot analyses were performed on various generations of pyrite from Qiucun. Selected trace metal compositions of different pyrite generations are illustrated in Figures 8 and 9. Representative time-resolved LA-ICP-MS spectra for each pyrite generation recorded during analyses are shown in Online Materials[1] Figure A1. Analytical results of different generations of pyrite are provided in Table 1 with median and median absolute deviation values. The full data sets are available in Online Materials[1] Table A3. The average detection limits obtained in this study are 0.8 ppm Co, 0.6 ppm Ni, 0.4 ppm Cu, 2.2 ppm Zn, 4.2 ppm As, 0.06 ppm Ag, 0.5 ppm Sb, 0.1 ppm Au, 0.05 ppm Bi, and 0.5 ppm Pb.

$Py_{1a}$ contains higher Co (median 27 ppm) and Ni (26 ppm) compared to $Py1_b$. Other elevated trace elements in $Py_{1a}$ include Ag (median 12 ppm), Pb (149 ppm), and Cu (4 ppm). Notably, $Py_{1a}$ has low Au (bdl−2.5 ppm, median 0.28 ppm) and highly variable As (5.9−5649 ppm, median 323 ppm) contents. In sharp contrast (Fig. 10), $Py_{1b}$ has much higher contents of As (median 6828 ppm), but other trace elements are generally very low compared to $Py_{1a}$ (e.g., median 12 ppm Co, 11 ppm Ni, 65 ppm Pb). The maximum Au and Ag contents in $Py_{1b}$ are 64 and 683 ppm, respectively.

The oscillatory-zoned $Py_{2a}$ consists of alternating As-rich and As-poor bands. The As-rich bands contain about an order of magnitude more As (median 5265 ppm) than the As-poor bands (1490 ppm As); similarly, Au (0.60−16 ppm) and Ag (3.1−1621 ppm) are at higher concentrations in these As-rich bands with respect to the As-poor bands (Au = bdl−1.9 ppm, Ag = bdl−216 ppm). Compared to $Py_{2a}$, $Py_{2b}$ is enriched in Au (median 31 ppm) and As (13 084 ppm). Note that the highest Au value (138 ppm) corresponds to the highest As content of 21 879 ppm.

### Trace element mapping of pyrite

LA-ICP-MS mapping was performed on three representative pyrite grains: (1) a pyrite grain representing $Py_{1a}$ and $Py_{1b}$ from Stage I (Fig. 10); (2) a typical oscillatory-zoned $Py_{2a}$ grain from Stage II (Fig. 11); and (3) a selected area containing $Py_{2a}$ and $Py_{2b}$ from Stage II (Fig. 12).

Figure 10 highlights two generations of a selected $Py_1$ grain: the porous and inclusion-rich core ($Py_{1a}$) has elevated Co, Ni, Ag, Pb, and Sb, whereas the overgrowth ($Py_{1b}$) has relatively high concentrations of Au and As compared to $Py_{1a}$. This map also confirms a positive correlation between As and Cu in $Py_{1b}$. The element map of one selected $Py_{2a}$ grain shows that the distributions of Au, As, Ag, Sb, and Tl correlate with the regular and continuous oscillatory zoning pattern displayed by the BSE image (Fig. 11). Zoning is sharply defined and is clearly visible as alternating broad bands of color. The bright zones are enriched in Au, As, Ag, Sb, and Tl compared to the darker bands, and these elements reach their highest concentrations in a fracture zone of the analyzed $Py_{2a}$ grain, which was corroded by later hydrothermal fluids. Co and Ni display very weak zonation, in which they are higher in the grain cores. Figure 12 indicates two generations of a selected pyrite grain from Stage II: the core ($Py_{2a}$) with apparent oscillatory zoning, whereas the thin outer rim ($Py_{2b}$) is enriched in Au, As, Ag, Sb, Tl, and Cu.

### In situ sulfur isotope data

The in situ sulfur isotope compositions for the different pyrite generations are presented in Online Materials[1] Table A4 and shown in Figure 13. In Stage I, 13 analyses of $Py_{1a}$ grains yielded a relatively restricted $\delta^{34}S$ range of –2.1 to 2.1‰ with

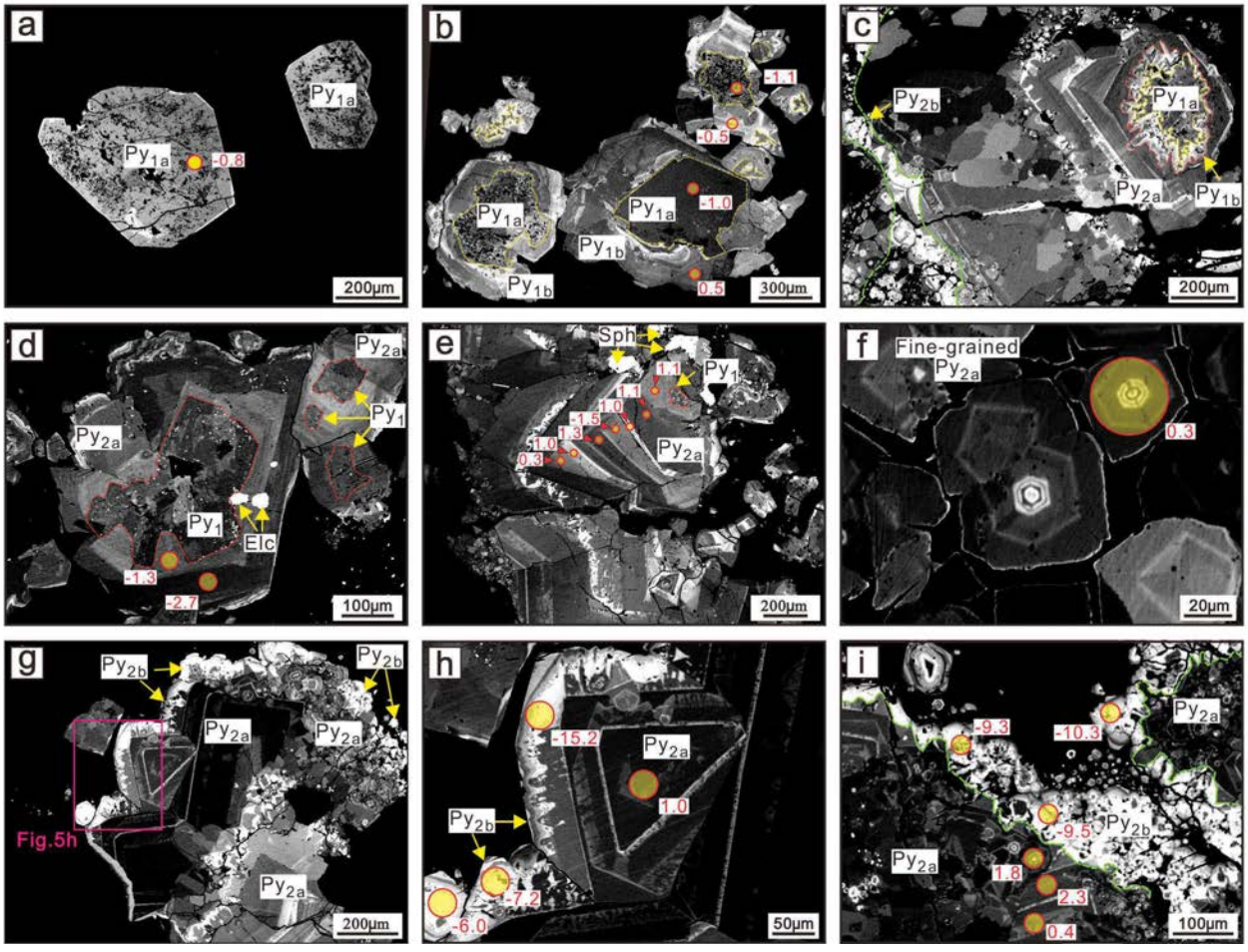


**Figure 5.** Backscattered-electron (BSE) images showing textural features and relationships of different generations of pyrite at Qiucun, also shown are the spots of in situ $\delta^{34}S_{V\text{-}CDT}$ (‰) isotope composition of pyrite: (**a**) $Py_{1a}$ with abundant silicate inclusions; (**b**) $Py_{1b}$ overgrowths on $Py_{1a}$; (**c**) early generation of sulfides, including $Py_{1a}$ and $Py_{1b}$, are overgrown by oscillatory-zoned $Py_{2a}$ and the outer rim of As-rich $Py_{2b}$ bands. Note that electrum in fracture of pyrite accompanied by quartz; (**d**) porous and inclusion-rich $Py_1$ is overgrown by oscillatory-zoned $Py_{2a}$, note that electrum filling the microfracture of the $Py_{2a}$; (**e**) $Py_{2a}$ with characteristic zoning; (**f**) cluster of euhedral fine-grained $Py_{2a}$ grains; (**g**–**i**) inclusion-free, zoned $Py_{2a}$ is surrounded by porous and As-rich $Py_{2b}$. Note that sharp and curvilinear interfaces among them. Abbreviations: Elc = electrum; Py = pyrite.

a mean value of –0.3‰, and 14 analyses of $Py_{1b}$ grains gave a similar $\delta^{34}S$ range of –3.6 to 1.3‰ (mean = –0.4‰). For Stage II, the $\delta^{34}S$ values of $Py_{2a}$ range from –3.2 to 4.6‰ (mean = 0.7‰, n = 39), which are significantly higher than those of $Py_{2b}$ with a range between –15.2 and –2.3‰ (mean = –7.3‰, n = 18).

## Discussion

### Pyrite formation and primary gold precipitation

**$Py_{1a}$.** Most $Py_1$ grains are composite grains with trace element-rich rims ($Py_{1b}$) and relatively trace element-poor cores ($Py_{1a}$) as highlighted by trace element images determined by LA-ICP-MS (Fig. 10). Overall, $Py_{1a}$ grains are enriched in Co and Ni and depleted in As and Au compared to $Py_{1b}$ (Fig. 8). The solubility of Co and Ni as chloride complexes in hydrothermal fluids is strongly positively correlated to temperature; for example, a decrease in temperature from 300 to 200 °C would cause a decrease in Co solubility by over two orders of magnitude (Migdisov et al. 2011). Deditius et al. (2014) established an exponential relation of As content in pyrite with temperature as:

$$C_{As} = 0.4785 \times e^{-0.0143T}$$

where $C_{As}$ is As content in mole percent (mol%) and $T$ is temperature (°C). Based on this equation, calculated concentrations of As increase from ~1000 ppm at 400 °C to ~20 000 ppm at 200 °C. Therefore, the variations in Co, Ni, and As may suggest that $Py_{1a}$ grains at Qiucun crystallized at higher temperatures than later pyrite generations. In addition, as shown in Figure 10, the region with high Co and Ni concentrations matches with the dark area (i.e., silicate inclusion-rich) on the BSE image; the silicate inclusions may also account for the high Co and Ni contents in $Py_{1a}$. Biotite phenocrysts in sub-volcanic host rocks at Qiucun were altered to chlorite and minor rutile. $Py_{1a}$ crystallized near or around the altered biotite (Online Materials[1] Fig. A2), which

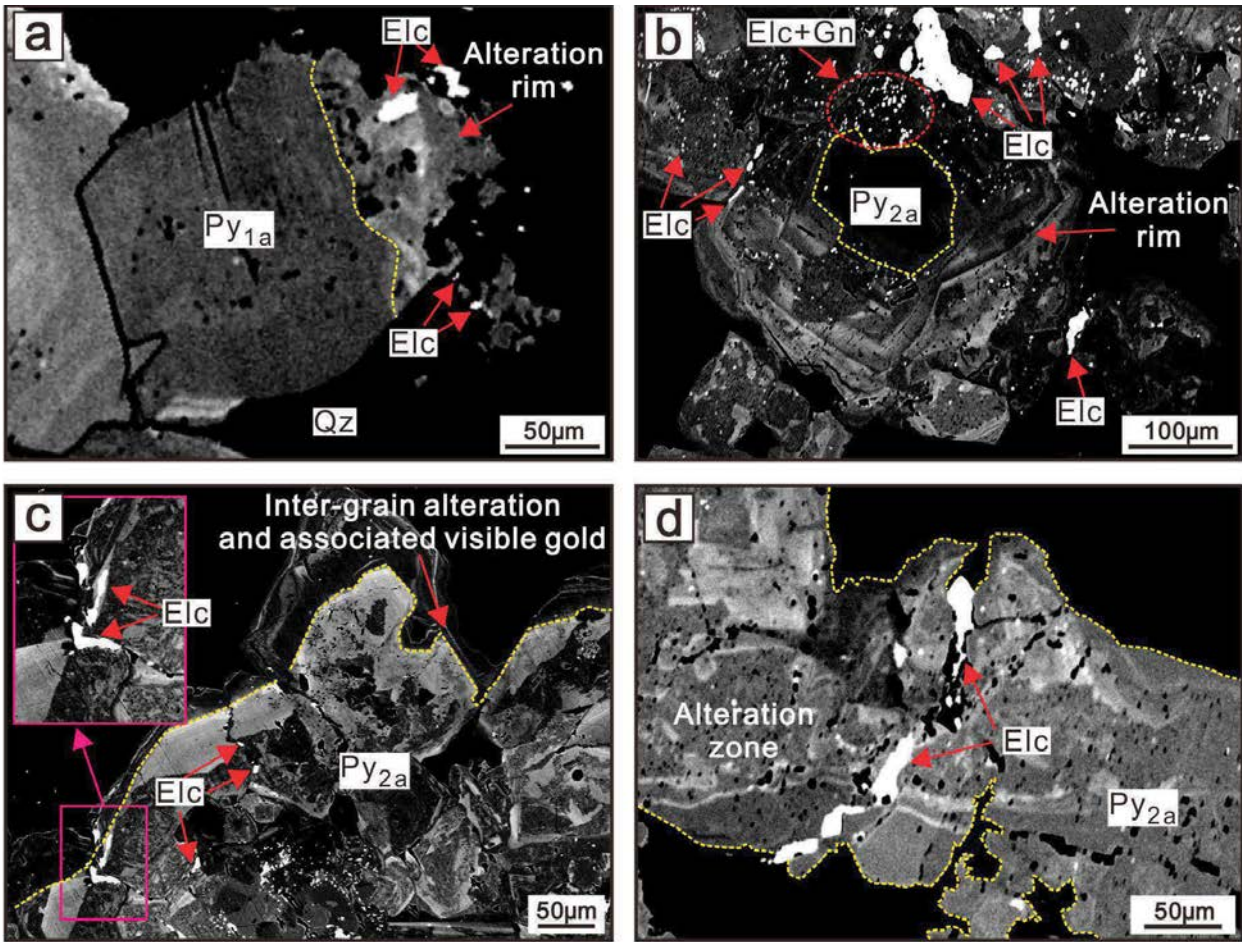


**Figure 6.** Collection of backscattered-electron images defining the characteristics of alteration zones within visible gold-bearing pyrite in the Qiucun gold deposit. (**a**) A pyrite grain from the Stage I vein showing the association later-stage between alteration rims and visible gold. (**b**) Anhedral $Py_{2a}$ grains showing advanced stages of post-formation alteration rim around the grain boundary. Visible electrum grains occur as inclusions in alteration rims, in fractures within them, or along grain boundaries. (**c**) Pyrite from the Stage II veins, showing intergrain rims and the association between alteration rims and visible gold. (**d**) Electrum filling the fractures of the altered $Py_{2a}$ grains. Abbreviations: Elc = electrum; Gn = galena; Py = pyrite; Qz = quartz.

contains abundant rutile inclusions, indicating that this alteration preceded $Py_{1a}$ precipitation. Sulfur was introduced via auriferous fluids, and that the chloritization of biotite provided the iron according to the reaction:

$$4KMgFe_2AlSi_3O_{10}(OH)_2 \text{ (biotite)} + 4H_2S + O_2 + 4H^+ \rightarrow 2Mg_2Fe_3Al_2Si_3O_{10}(OH)_8 \text{ (chlorite)} + 2FeS_2 \text{ (pyrite)} + 6SiO_2 + 2H_2O + 4K^+$$

Ti dissolved from biotite quickly precipitated as rutile in and around the altered biotite. Other minerals that make up the alteration paragenesis of sub-volcanic rocks also occur as inclusions in $Py_{1a}$, which also supports the hypothesis that $Py_{1a}$ was formed via fluid-wall rock interaction. The formation of open space during the replacement of biotite by pyrite can be explained by considering the different densities of these minerals (biotite = 3.09 g/cm$^3$; pyrite = 5.01 g/cm$^3$). Assuming that all Fe in pyrite is derived from biotite, the molar volume of the resulting pyrite will be significantly lower than that of biotite. This process may also explain the presence of abundant silicate inclusions in $Py_{1a}$.

**Gold in $Py_{1a}$.** $Py_{1a}$ contains minor amounts of invisible gold (~2.5 ppm), which precipitated contemporaneously with the very first pyrite generation in the vein stock and wall rock. Sulfur isotope ratios ($\delta^{34}S$ = –2.1 to 2.1‰) and the absence of sulfates and hematite suggest that $H_2S$ was the predominant sulfur species in the ore fluid during pyrite formation; therefore, $AuHS_2^-$ is likely to have been the major gold-transporting complex (Ohmoto 1972). As discussed above, $Py_{1a}$ formed at the expense of biotite. Thus, the destabilization of gold bisulfide complexes due to loss of $H_2S$ from the ore fluid during sulfidation of the wall rocks was the most likely mechanism for gold deposition (Williams-Jones et al. 2009). The time-invariant trace of the spot analysis and the positive correlation between As and Au indicate that Au and As are most likely contained as solid solution or as nanoparticles in $Py_{1a}$ rather than as inclusions of free gold (Fig. 7a; Reich et al. 2005; Gregory et al. 2016).

**$Py_{1b}$ and $Py_{2a}$.** The rims of $Py_1$ ($Py_{1b}$) are significantly enriched in As, Au, and Cu compared to their cores (Fig. 10). $Py_{1b}$

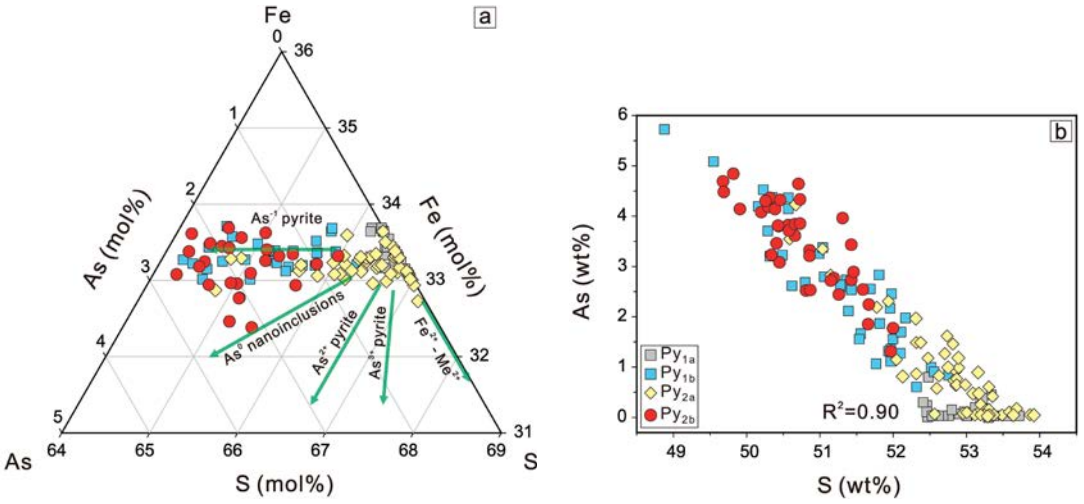


**Figure 7.** (**a**) Ternary diagram showing the As-Fe-S composition of pyrite; only EPMA data were considered. Five different trends show substitution of (1) As for S ($As^{-1}$ pyrite); (2) $As^0$ nano-inclusions; (3) $As^{2+}$ for Fe ($As^{2+}$ pyrite); (4) $As^{3+}$ for Fe ($As^{3+}$ pyrite); and (5) divalent metals ($Me^{2+}$) substituting isovalently for Fe (after Deditius et al. 2008, 2014). (**b**) A plot of As vs. S concentrations for the pyrite, showing a good linear inverse correlation between these elements.

has delicate banded textures related to elevated trace element concentrations, and many of the $Py_{1b}$ crystals appear to have overgrown irregular and corroded $Py_{1a}$ grains (Fig. 5b). Some of the $Py_{1b}$ grains are truncated by grain boundaries (Fig. 5b), consistent with the partial dissolution of pyrite (Cook et al. 2009). After $Py_1$ formation, oscillatory-zoned $Py_{2a}$, accompanied by a few quartz crystals, precipitated during Stage II (Figs. 5c–5f). Oscillatory zoning, a common feature in auriferous pyrite, has been documented in many gold deposits (e.g., Peterson and Mavrogenes 2014). Periodic and repetitive changes in pressure (*P*), temperature (*T*), and bulk fluid composition have been invoked to explain this zoning (Velásquez et al. 2014). Episodic fluctuations in fluid compositions from multiple hydrothermal events generally lead to several stages of pyrite precipitation with distinct sulfur isotope compositions, irregular boundaries, and corrosion textures between alternating bands (Barker et al. 2009). None of these features has been observed in the $Py_{2a}$, ruling out a multi-stage pyrite crystallization model. Instead, episodic changes of physicochemical parameters (e.g., *P*-*T*-pH) during the boiling of the ore fluids are invoked.

Previous studies suggested that zoning in pyrite reflected rapid variations in the As content of ore fluids through time (Deditius et al. 2014; Velásquez et al. 2014). Ballantyne and Moore (1988) proposed that the As concentration of hydrothermal fluids is inversely proportional to the partial pressure of $H_2S$ in geothermal systems and their fossil analogs, the epithermal deposits. The Qiucun hydrothermal system was relatively shallow, and repeated boiling is manifested in hydrothermal breccias and hydraulic fracturing and in the features of auriferous veins (colloform banded and vuggy quartz veins and bladed calcite crystals) and fluid inclusions (Ni et al. 2018). In such a system, rapid fluctuations in pressure, from hydrostatic to lithostatic, could have been caused by fracturing and resealing of fluid conduits. These variations, and the accompanying boiling, could also contribute to the rapid changes in pH and variations and the activity of sulfur, thus in the solubility of As in the ore fluid (e.g., Kouzmanov and Pokrovski 2012). Moreover, the removal of volatiles ($H_2S$ and $CO_2$) into vapor tends to increase the pH of

**Table 1.** Statistic values of LA-ICP-MS analyses of each pyrite generation from the Qiucun gold deposit

| Pyrite generations | Statistical parameters | Au | Co | Ni | Cu | Zn | As | Se | Ag | Sb | Te | Hg | Tl | Bi | Pb |
|---|---|---|---|---|---|---|---|---|---|---|---|---|---|---|---|
| $Py_{1a}$ | Min | bdl | bdl | 0.81 | bdl | bdl | 5.9 | bdl | bdl | bdl | bdl | bdl | bdl | bdl | bdl |
| $n$ = 32 | Max | 2.5 | 590 | 368 | 1088 | 527 | 5649 | 8.0 | 197 | 293 | 11 | 0.96 | 3.2 | 31 | 3969 |
| | Med | 0.28 | 27 | 26 | 40 | 1.5 | 343 | 2.3 | 12 | 7.0 | 0.4 | 0.00 | 0.04 | 0.29 | 149 |
| | MAD | 0.22 | 26 | 24 | 39 | 1.4 | 323 | 1.2 | 10 | 6.4 | 0.4 | 0.00 | 0.04 | 0.28 | 148 |
| $Py_{1b}$ | Min | bdl | bdl | bdl | bdl | bdl | 1112 | bdl | 0.67 | bdl | bdl | bdl | bdl | bdl | 0.59 |
| $n$ = 25 | Max | 64 | 212 | 151 | 1052 | 261 | 32787 | 9.5 | 483 | 7915 | 5.5 | 23 | 620 | 18 | 2137 |
| | Med | 1.4 | 12 | 11 | 48 | 1.1 | 6828 | 2.4 | 16 | 26 | 0.2 | 0.07 | 0.33 | 0.02 | 65 |
| | MAD | 1.4 | 11 | 9.8 | 42 | 0.65 | 5272 | 1.5 | 11 | 24 | 0.2 | 0.07 | 0.32 | 0.02 | 57 |
| $Py_{2a}$ | Min | bdl | bdl | bdl | bdl | bdl | 109 | bdl | bdl | bdl | bdl | bdl | bdl | bdl | bdl |
| $n$ = 36 | Max | 16 | 73 | 107 | 1362 | 66 | 17469 | 12 | 1621 | 4771 | 45 | 96 | 504 | 2.4 | 4733 |
| | Med | 1.7 | 4.6 | 18 | 42 | 0.92 | 3123 | 1.0 | 25 | 77 | 0.3 | 0.07 | 0.89 | 0.03 | 66 |
| | MAD | 1.5 | 4.6 | 18 | 41 | 0.67 | 1890 | 1.0 | 22 | 68 | 0.3 | 0.07 | 0.88 | 0.02 | 57 |
| $Py_{2b}$ | Min | 1.5 | bdl | bdl | bdl | bdl | 5851 | bdl | 6.8 | 7.7 | bdl | bdl | bdl | bdl | 5.2 |
| $n$ = 19 | Max | 138 | 106 | 55 | 579 | 20 | 21879 | 7.1 | 1626 | 2176 | 5.5 | 3.4 | 188 | 0.41 | 389 |
| | Med | 31 | 3.2 | 3.4 | 276 | 1.3 | 13084 | 3.1 | 40 | 68 | 0.2 | 0.03 | 0.30 | 0.01 | 63 |
| | MAD | 29 | 3.2 | 3.3 | 182 | 1.1 | 2941 | 0.71 | 29 | 39 | 0.2 | 0.03 | 0.22 | 0.01 | 36 |

*Notes*: All data are presented in ppm. Abbreviations: bdl = below detection limit; Min = minimum value; Max = maximum value; Min = minimum value; MAD = median absolute deviation; $n$ = number of analysis.

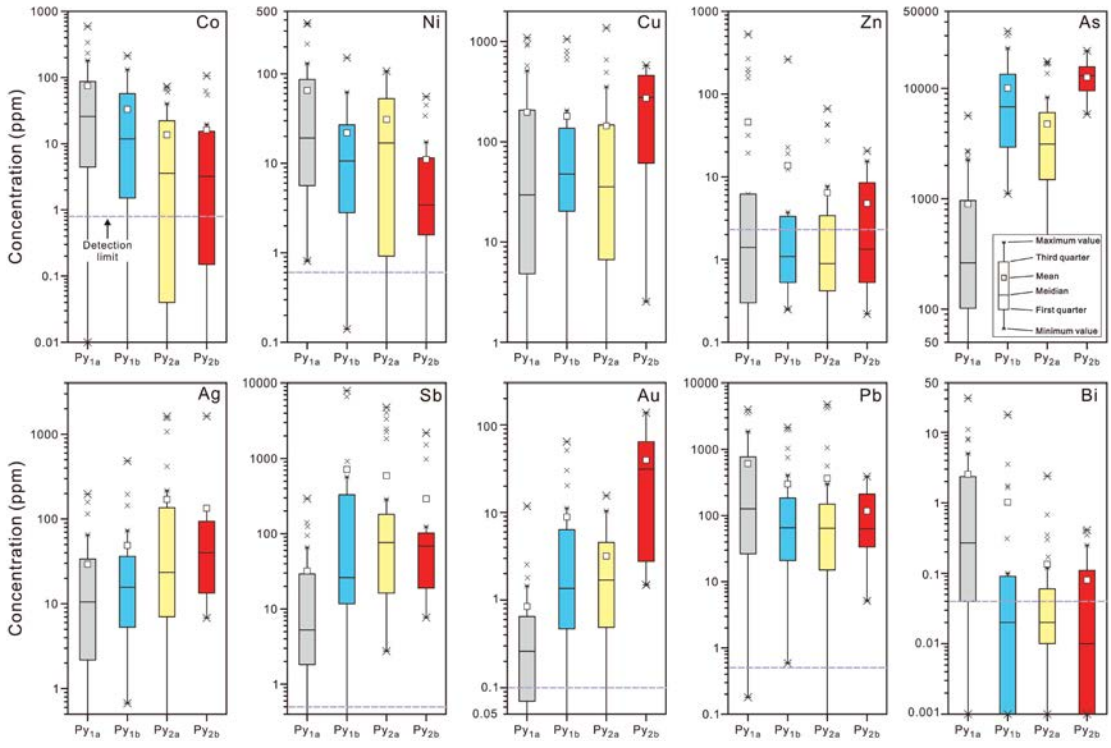


**Figure 8.** Trace element distribution diagram showing the variation in the Co, Ni, Cu, Zn, As, Ag, Sb, Au, Pb, and Bi concentrations (in ppm) for all pyrite generations. Concentrations are in logarithmic scale.

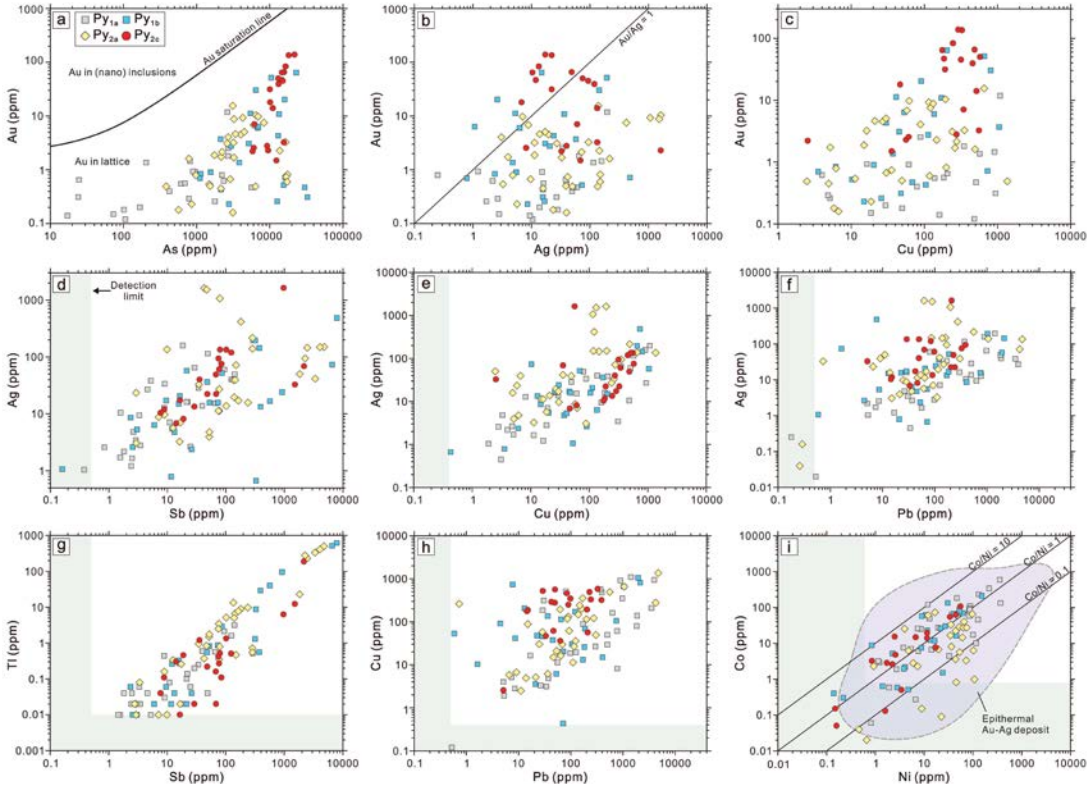


**Figure 9.** Elemental concentration scatterplots for different generations of pyrite from the Qiucun deposit. (**a**) Au vs. As: almost all the pyrite generations show a positive relationship with Au-As. All the data spots are below the gold solubility line in pyrite (Reich et al. 2005); (**b**) Au vs. Ag; (**c**) Au vs. Cu; (**d**) Ag vs. Sb; (**e**) Ag vs. Cu; (**f**) Ag vs. Pb; (**g**) Tl vs. Sb; (**h**) Cu vs. Pb; (**i**) Co vs. Ni.

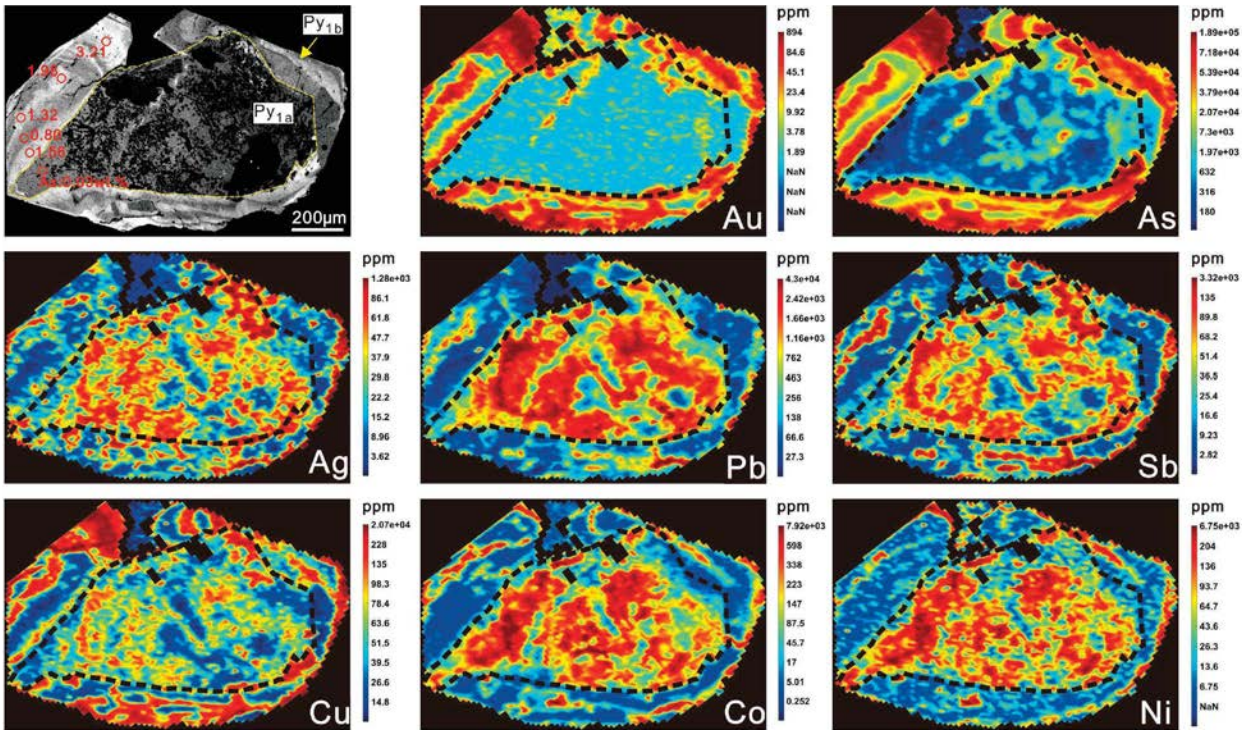


**Figure 10.** LA-ICP-MS element maps with logarithmic color scales (in ppm) showing contents and distribution patterns of trace elements of a representative pyrite grain from Stage I. Numbers on BSE image represent wt% As.

the solution, which decreases the solubility of sulfides. Therefore, the cyclicity of pyrite banding reflects repeated and sudden variations in fluid pressure and transient fluid flow regimes.

**Gold in $Py_{1b}$ and $Py_{2a}$.** Rims of $Py_1$ and the oscillatory-zoned $Py_{2a}$ all contain invisible gold, as is the case for $Py_1$ cores. However, the As-rich bands in $Py_{1b}$ and oscillatory-zoned $Py_{2a}$ have about one to two magnitudes more Au than the $Py_{1a}$, whereas the As-poor bands contain less Au than $Py_{1a}$. This relationship is also well-revealed by LA-ICP-MS images, an apparent Au enrichment coinciding with As-rich bands in these pyrite generations (Figs. 11–12). There is also a positive correlation between As and Au (Fig. 9a), which is consistent with the preferential precipitation of gold in As-rich layers (e.g., Deditius et al. 2014). It is generally accepted that As-rich sulfides play an important role in scavenging gold (Simon et al. 1999). Fluid boiling at moderate temperatures as documented for Qiucun (<250 °C; Ni et al. 2018) is a very efficient way of precipitating most minerals from the liquid phase (Heinrich 2007). As, Au, Fe, and most other metallic elements exhibit vapor-liquid partitioning coefficients mainly in favor of the liquid phase at temperatures below 300 °C (Kouzmanov and Pokrovski 2012), and thus precipitate from the liquid phase if the extent of phase separation is high enough to remove a sufficient part of $H_2O$ into the vapor and thus supersaturate the liquid with arsenian pyrite and native gold.

### Secondary gold enrichment

**Formation of gold- and trace element-rich $Py_{2b}$.** Coupled dissolution-reprecipitation (CDR) reactions have proven significant for the remobilization and upgrading of sulfide-hosted gold ores in various types of gold deposits (Sung et al. 2009; Hastie et al. 2020). Later hydrothermal fluids dissolve parts of the parent mineral in the CDR processes and precipitate a compositionally different daughter phase at nanometer scale. The resulting product is characterized by high porosity and preserves the external shape and crystallographic orientation of the replaced grain (Putnis 2009). Textural observations suggest that porous $Py_{2b}$ occurs preferentially along microfractures and grain margins of $Py_{2a}$ (Figs. 5g–5i). The reaction front is sharp and curvilinear (Fig. 5h), which is strong evidence of CDR reactions (Putnis 2009). These textures suggest a fluid dissolved earlier $Py_{2a}$, which was then re-precipitated as $Py_{2b}$. Preservation of the external morphology of parent $Py_{2a}$ (Figs. 5g–5i) indicates some degree of a spatial and temporal coupling between the dissolution and re-precipitation (Wu et al. 2019).

The in situ LA-ICP-MS analyses in the spot- and mapping-modes highlight systematic trace element variations between different pyrite generations in Stage II veins (Figs. 8–9 and 12). During the replacement of $Py_{2a}$ by porous $Py_{2b}$, elements concentrated in $Py_{2b}$ relative to $Py_{2a}$ (Au, As, Ag, Sb, Pb, Tl, and Cu) might be sourced from infiltrating fluids or from sulfides hosted in sub-micrometer inclusions (e.g., electrum, galena, chalcopyrite, and arsenopyrite) formed during remobilization from earlier pyrite generations. The peaks of $^{65}Cu$, $^{121}Sb$, $^{197}Ag$, and $^{208}Pb$ in LA-ICP-MS laser profiles (Gregory et al. 2016; Online Materials[1] Fig. A1f) support the existence of such sub-microscopic sulfide inclusions in $Py_{2b}$. The presence of Au-, Cu-, Pb-, Ag-, and Sb-bearing minerals in later alteration pyrite-arsenopyrite assemblages formed through trace element remobilization and

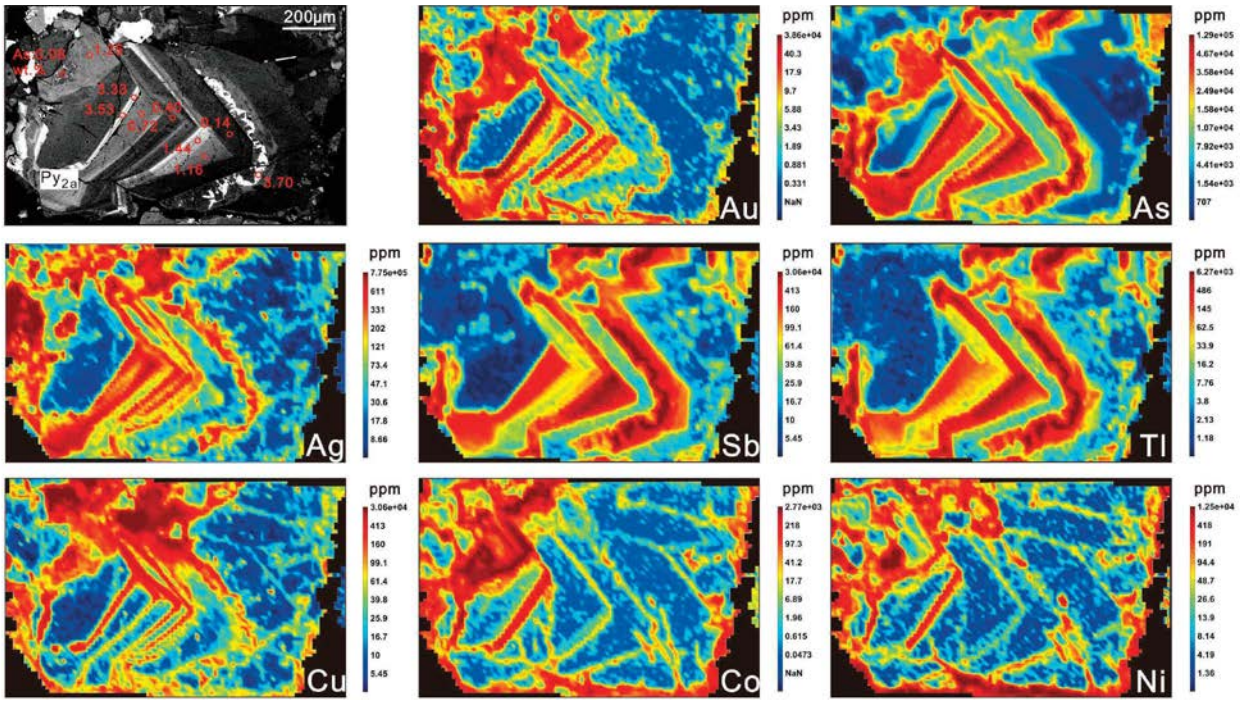


**Figure 11.** Elemental maps generated with LA-ICP-MS which show the distributions of selected trace elements in an oscillatory zoned $Py_{2a}$ crystal from the Qiucun deposit.

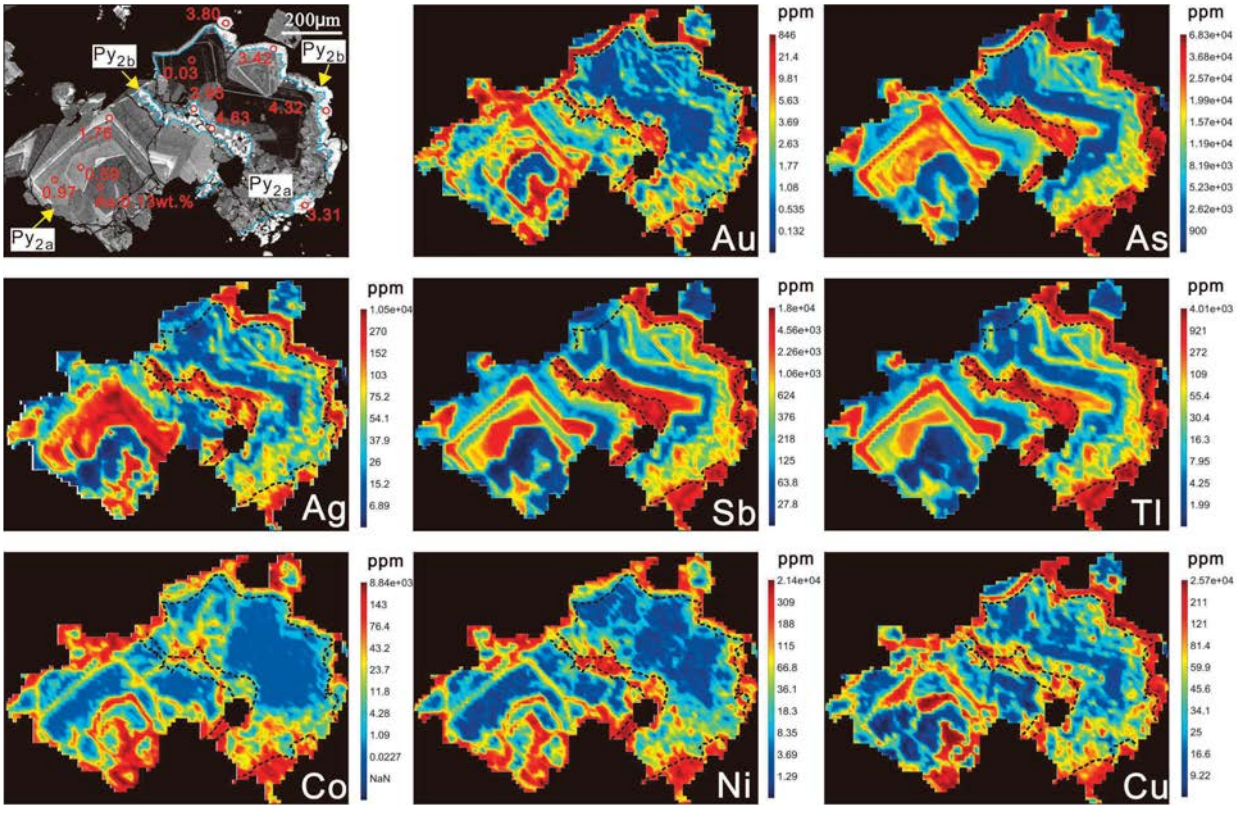


**Figure 12.** Elemental maps generated with LA-ICP-MS which show the distributions of selected trace elements in $Py_2$ aggregate in Stage II vein from the Qiucun deposit.

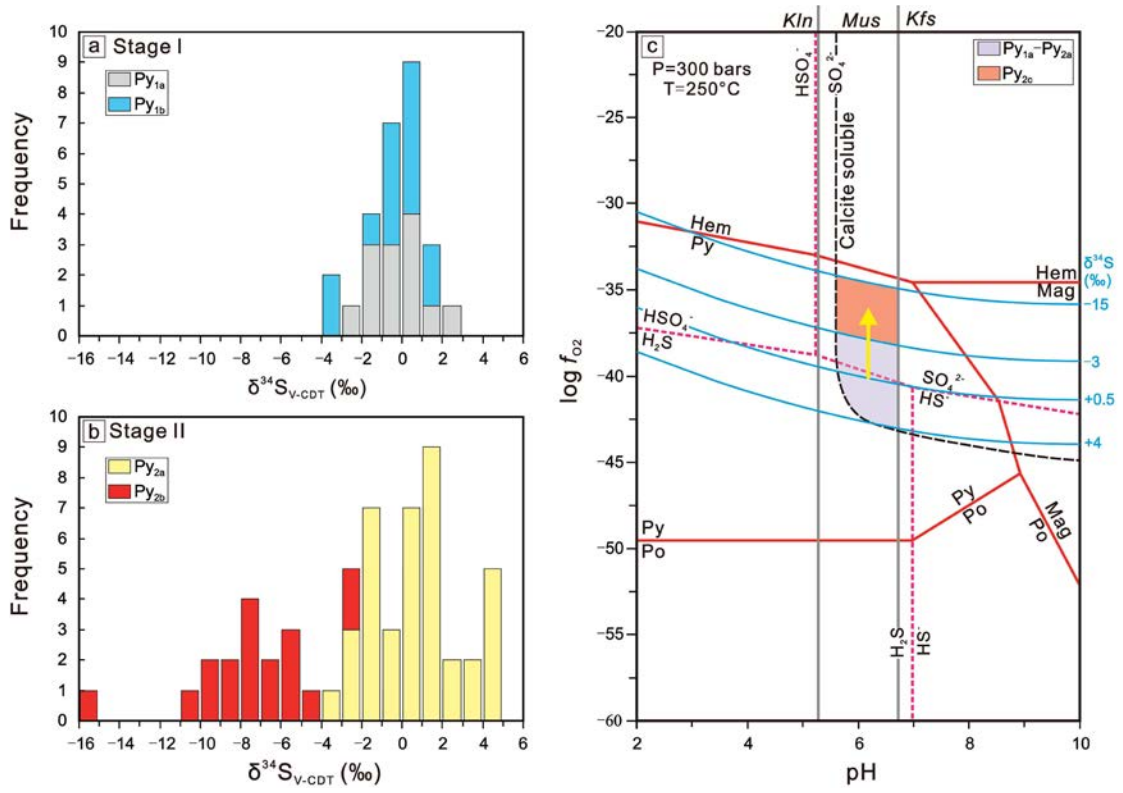


**Figure 13.** Histograms showing the distribution of $\delta^{34}S$ values of different generations of pyrite in Stage I (**a**) and Stage II (**b**). (**c**) Log $f_{O_2}$–pH diagram showing stability relationships in the Fe-O-S system and alteration assemblages for gold mineralization in the Qiucun deposit at 250 °C. The diagrams show the predominance boundaries of aqueous sulfur species (pink dashed), mineral stability in the Fe-O-S system (red solid), alteration equilibra (gray solid), and calcite dissolution (black dashed). The sulfur isotope counters are indicated by blue lines (after Ohmoto 1972 and Zhai et al. 2020).

secondary enrichment during CDR reactions has also been documented in many other gold deposits (e.g., Sung et al. 2009; Hastie et al. 2020).

**Visible gold in pyrite ores.** Cycles of hydrothermal infiltration during ore deposit formation can alter pre-existing ore minerals and remobilize gold, among other chemical constituents (e.g., Morey et al. 2008; Cook et al. 2013). For example, visible gold concentrated around the grain boundaries and fractures of pyrite and arsenopyrite is very common in orogenic gold deposits worldwide. It has been interpreted to form via the hydrothermal alteration of pre-existing auriferous sulfides during an increase in temperature and sulfur fugacity during prograde metamorphism (Morey et al. 2008; Lawley et al. 2017). For example, at Sunrise Dam, Australia, textural evidence exists that is consistent with the replacement of arsenian pyrite, whereby remobilized gold was deposited as native gold inclusions oriented parallel to crystal faces or in fractures, inferring the partial replacement of parent arsenian pyrite via fluid-mediated CDR reactions (Sung et al. 2009). Furthermore, oscillatory- and sector-zoned pyrite from Jerome and Kenty deposits in Canada record textures, such as porosity development coincident with the presence of native gold and accessory sulfide phases, that are suggestive of CDR reactions that liberated gold and associated elements from earlier auriferous pyrite (Hastie et al. 2020).

At Qiucun, visible electrum grains occur as inclusions within all pyrite generations, as solitary grains or veins in fractures at grain boundaries in pyrite (Fig. 6). The visible gold-bearing pyrite grains (Fig. 6) are pervasively fractured have irregular grain boundaries, and BSE images reveal that these pyrite grains have intra-granular compositional zones that are possibly related to a dynamic alteration history. Parallel to the fractures and boundaries or intra-grain narrow composite rims within the auriferous pyrite are characterized by a higher-than-average atomic mass (Fig. 6). These rims vary in their dimensions but are, in general, up to 300 μm in thickness from grain boundaries and fracture margins. As shown in Figures 6a–6c, the rims are porous and define zones in which selective chemical modification of the preexisting pyrite parallel to fracture-grain boundaries has taken place. This grain boundary-fracture association indicates an external (i.e., post-formation) influence. Due to the lack of other mineral phases containing As and S, the infiltration of a later hydrothermal fluid is considered responsible. This fluid would have infiltrated along grain boundaries, possibly promoting fracturing and facilitating the reaction process. The resulting pyrite rims are thus thought to be alteration rims.

The precipitation of invisible gold, followed by the later formation of visible gold, is schematically illustrated in Figure 14. Given that primary pyrite grains are characterized by relatively

uniform invisible gold within single generations, and that alteration rims (which replaced primary growth phases) are depleted in invisible gold, it is suggested that early refractory gold exsolved and was then remobilized locally to form at least part of the later visible gold. The formation of visible gold by hydrothermal alteration of refractory gold-bearing pyrite may provide new insights into the formation of high-grade gold ores in epithermal deposits, although the direct introduction of gold by later auriferous fluids cannot be ruled out. It is suggested here that fluids reacted with fractured auriferous pyrite, causing CDR reactions during repeated, episodic brittle deformation events. Invisible gold, together with some of the low-melting-point elements (e.g., Cu, Pb, and Sb), were dissolved and re-precipitated as visible gold, galena, and chalcopyrite, within the same pyrite grain as inclusions, as well as in fractures within pyrite (Fig. 14).

### Sulfur isotopic fingerprint of ore-forming processes

Early pyrite generations ($Py_{1-2a}$) from the auriferous veins at Qiucun yielded a narrow range of $\delta^{34}S_{py}$ of –3.6 to 4.6‰ with an average of 0.3‰, independent of pyrite generation (Figs. 13a–13b). The temperature of the ore fluid at Qiucun is thought to be within the range of 180 to 250 °C based on microthermometry of fluid inclusions in the quartz from vein-type ores (Ni et al. 2018). Assuming a temperature of 250 °C, the corresponding range and mean $\delta^{34}S_{H_2S}$ values are –5.1 to 3.1‰ and –1.2‰, respectively. The $\delta^{34}S$ values reported here are also very close to those in nearby magmatic-hydrothermal deposits (e.g., the Ancun, Xiaban, Dongyang Au deposits), which are generally in the range of –4 to 2‰ (Li et al. 2018a, 2018b). This demonstrates that most of the gold deposits in the Dehua goldfield had a similar magmatic sulfur source. The Co and Ni contents reported here for pyrite from the Qiucun deposit are similar to those in epithermal Au-Ag hydrothermal systems (Fig. 9i). The dominant range of Co/Ni ratios between 0.5 and 10 is consistent with pyrite of a magmatic-hydrothermal origin (Reich et al. 2016).

There is a very slight variation of $\delta^{34}S$ values (–1.5 to 1.3‰) in a single oscillatory-zoned $Py_{2a}$ grain (Fig. 5e), illustrating a systematic decoupling from the trace element distribution, which was controlled by pressure fluctuations and repeated localized fluid boiling as discussed earlier. Previous studies have suggested that $\delta^{34}S$ ratios of sulfide minerals are strongly influenced by oxygen fugacity ($f_{O_2}$), pH, temperature, and the composition of the parental fluid, but the pressure effect is limited (e.g., Ohmoto 1972; Seal 2006; Li et al. 2018). Therefore, the localized pressure fluctuations and subsequent fluid boiling were not enough to generate sulfur isotope fractionation in oscillatory-zoned pyrite grains. However, the in situ $\delta^{34}S$ ratios for the $Py_2$ rims ($Py_{2b}$: –15.2 to –2.3‰) are distinctly lighter than the cores in all the analyzed samples: the average $Py_{2b}$ is 8.0‰ lighter than the $Py_{2a}$. The negative $\delta^{34}S$ values in $Py_{2b}$ either reflect a sulfur source contribution of negative $\delta^{34}S$ from the sedimentary host rocks or isotopic fractionation due to change of temperature and oxygen fugacity along with the evolution of the ore fluids. Because no significant amount of negative $\delta^{34}S$ sedimentary rocks have been found in any lithological unit in the Dehua gold field, we consider changes in the physicochemical conditions (e.g., temperature, pH, and $f_{O_2}$; Ohmoto 1972; Ma et al. 2021b) during pyrite precipitation is a likely explanation for the negative $\delta^{34}S$ values of $Py_{2b}$. During main-stage pyrite mineralization, a shift from sericite to illite alteration (Ni et al. 2018) reflects the cooling of the ore fluid. Pyrite is estimated to be 1.5‰ heavier than $H_2S$ in the hydrothermal fluid at 250 °C, whereas the pyrite-$H_2S$ fractionation is about 1.9‰ at 180 °C (Ohmoto and Rye 1979). Cooling of the ore fluid by 70 °C could cause a ~0.4‰ increase in pyrite $\delta^{34}S$, and therefore, temperature decrease alone cannot explain the observed decrease in $\delta^{34}S$ ratios in $Py_{2b}$. The pH of

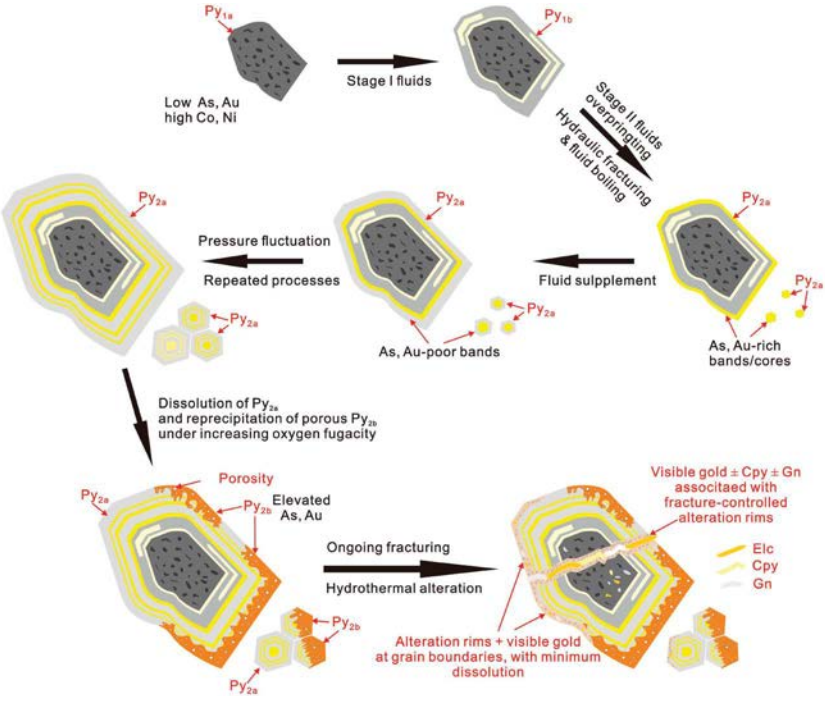


**Figure 14.** A cartoon illustrating a model for pyrite formation and gold re-enrichment at Qiucun. See text for explanations.

Stage II vein formation had a narrow range of 5.6 to 6.7, based on the observation that the mineralization was associated with sericite-illite alteration and the occurrence as a gangue mineral (Ni et al. 2018). Thus, the pH value should not significantly affect the sulfur isotopic composition either.

More significant changes in $\delta^{34}S$ ratios can result from changes in the proportions of oxidized and reduced sulfur species in the ore fluid (e.g., Ohmoto 1972). Fluid oxidation has been commonly suggested to cause negative $\delta^{34}S$ ratios in sulfides and rapid gold deposition in hydrothermal ore deposits (LaFlamme et al. 2018). Fractionation of heavy $^{34}S$ into the oxidized sulfur species would cause $^{34}S$-depleted $H_2S$ in the residual hydrothermal fluid. Consequently, pyrite deposited from the fluid after oxidation would be characterized by much lower $\delta^{34}S$ ratios relative to pyrite precipitated before oxidation (Ohmoto 1972). At the shallow crustal levels recorded at Qiucun (~260 m; Ni et al. 2018), it is suggested that during the later mineralization stage cooler and oxidized meteoric water was increasingly involved in the precipitation of the last generation of pyrite ($Py_{2b}$), leading to the further oxidation of the mineralizing fluids and consequently lowering of $\delta^{34}S$ (Fig. 13).

## Implications

In this contribution, two main types of Au mineralization are recognized at Qiucun, with distinctly different mechanisms. The first is the primary precipitation of invisible gold within unaltered pyrite domains ($Py_{1a}$, $Py_{1b}$, and $Py_{2a}$). We relate the textural and geochemical features of these pyrites to their depositional mechanisms: $Py_{1a}$ with low concentrations of As and Au is contemporary with the early hydrothermal alteration of biotite in the host rock and commonly occurs as cores of pyrite. The $Py_{1b}$ and $Py_{2a}$ with characteristics oscillatory zoning of As and Au formed at Stages I–II. This oscillatory zoning is interpreted to have resulted from pressure fluctuations and repeated fluid boiling around the pyrite crystals. Invisible gold is present throughout these pyrite crystals but is more abundant in the As-rich bands. The second mechanism is the secondary enrichment of visible and invisible gold (hosted by $Py_{2b}$) associated with later-stage alteration events produced chemically modified alteration rims on the auriferous pyrite. Results of LA-ICP-MS analyses suggest that Au and other trace elements (As, Ag, Sb, Pb, Tl, and Cu) that had been initially incorporated in $Py_{2a}$ were partly expelled and remobilized during replacement of porous and trace element (including Au)-rich $Py_{2b}$. The very low $\delta^{34}S$ values recorded by $Py_{2b}$ suggest the partial dissolution of $Py_{2a}$ and re-precipitation of $Py_{2b}$ under increasing oxygen fugacity. An additional consequence of the reactivation process is the fracturing of the previously formed auriferous pyrite that continued through later brittle deformation events, which led to more fracturing of pyrite. This newly created porosity of pyrite facilitated further fluid flow along the margins of fractures and grain boundaries within pyrite, including hydrothermal alteration of pyrite and dissolution of invisible gold, which re-precipitated as small inclusions and in fractures as larger veins. This study highlights that the textural, geochemical, and sulfur isotopic compositions of pyrite can provide critical information not only for the physicochemical conditions of the initial gold deposition but also for the secondary invisible and visible gold enrichment processes in Au deposits.

## Acknowledgments

Our thanks extend to the Qiucun Mining Ltd. and the Fujian Institute of Geological Survey and Research for providing access to samples and information about the deposit. Kui-Dong Zhao, Wei Chen, Fang-Yue Wang, Jian-Feng Gao, Liang Li, and Pei-Jun Lin are also thanked for their help with lab work. Constructive reviews by Daniel Gregory and Xing-Hui Li, and editorial comments and suggestions by editor Matthew Steele-MacInnis have been very helpful in our revision and are gratefully acknowledged.

## Funding

This study was supported by the National Natural Science Foundation of China (grant no. 41973044), the MOST Special Fund from the State Key Laboratory of Geological Processes and Mineral Resources, China University of Geosciences (grant no. MSFGPMR03-2), and the Fundamental Research Funds for National Universities, China University of Geosciences (Wuhan) (grant no. 2201610076). We certify that we have no potential conflicts of interest including relevant financial interests.

## References cited

Ballantyne, J.M., and Moore, J.N. (1988) Arsenic geochemistry in geothermal systems. Geochimica et Cosmochimica Acta, 52, 475–483.

Barker, S.L.L., Hickey, K.A., Cline, J.S., Dipple, G.M., Kilburn, M.R., Vaughan, J.R., and Longo, A.A. (2009) Unlocking invisible gold: Use of nanoSIMS to evaluate gold, trace elements, and sulfur isotopes in pyrite from Carlin-type gold deposits. Economic Geology, 104, 897–904.

Cook, N.J., Ciobanu, C.L., and Mao, J.W. (2009) Textural control on gold distribution in As-free pyrite from the Dongping, Huangtuliang, and Hougou gold deposits, North China craton (Hebei Province, China). Chemical Geology, 264, 101–121.

Cook, N.J., Ciobanu, C.L., Meria, D., Silcock, D., and Wade, B. (2013) Arsenopyrite-pyrite association in an orogeni gold ore: Tracing mineralization history from textures and trace elements. Economic Geology, 108, 1273–1283.

Deditius, A., Utsunomiya, S., Reich, M., Kesler, S., Ewing, R., Hough, R., and Walshe, J. (2011) Trace metal nanoparticles in pyrite. Ore Geology Reviews, 42, 32–46.

Deditius, A.P., Reich, M., Kesler, S.E., Utsunomiya, S., Chryssoulis, S.L., Walshe, J.L., Hough, R., and Ewing, R.C. (2014) The coupled geochemistry of Au and As in pyrite from hydrothermal ore deposits. Geochimica et Cosmochimica Acta, 140, 644–670.

Fan, K. (2015) Geological characteristics and prospecting direction of Qiucun gold mine in Dehua county, Fujian province. Modern Mining, 560, 84–86 (in Chinese with English abstract).

Franchini, M., McFarlane, C., Maydagán, L., Reich, M., Lentz, D.R., Meinert, L., and Bouhier, V. (2015) Trace metals in pyrite and marcasite from the Agua Rica prophyry-high sulfidation epithermal deposit, Catamarca, Argentina: Textural features and metal zoning at the porphyry to epithermal transition. Ore Geology Reviews, 66, 366–387.

Gao, J.F., Jackson, S.E., Dube, B., and De Souza, S. (2015) Genesis of the Canadian Malartic, Côté Gold, and Musselwhite gold deposits: Insights from LA-ICP-MS element mapping of pyrite. In B. Dubé and P. Mercier-Langevin, Eds., Targeted Geoscience Initiative 4: Contributions to the Understanding of Precambrian Lode Gold Deposits and Implications for Exploration, p. 157–175. Geological Survey of Canada, Open File 7852.

Gregory, D.D., Large, R.R., Bath, A.B., Steadman, J.F., Wu, S., Danyushevsky, L., Bull, S.W., Holden, P., and Ireland, T.R. (2016) Trace element content of pyrite from the Kapai Slate, St. Ives Gold District, Western Australia. Economic Geology, 111, 1297–1320.

Gregory, D.D., Cracknell, M.J., Large, R.R., McGoldrick, P., Kuhn, S., Maslennikov, V.V., Baker, M.J., Fox, N., Belousov, I., Figueroa, M.C., and others (2019) Distinguishing ore deposit type and barren sedimentary pyrite using laser ablation-inductively coupled plasma-mass spectrometry trace element data and statistical analysis of large data sets. Economic Geology, 114, 771–786.

Gopon, P., Douglas, J.A., Auger, M.A., Hansen, L., Wade, J., Cline, J.S., Robb, L.J., and Moody, M.P. (2019) A nanoscale investigation of Carlin-type gold deposits: An atom-scale elemental and isotopic prospective. Economic Geology, 114, 1123–1133.

Gourcerol, B., Kontak, D.J., Thurston, P.C., and Petrus, J.A. (2018) Results of LA-ICP-MS sulfide mapping from Algoma-type BIF gold systems with implications for the nature of mineralizing fluids, metal sources, and deposit models. Mineralium Deposita, 53, 871–894.

Haroldson, E.L., Beard, B.L., Satkoski, A.M., Brown, P.E., and Johnson, C. (2018) Gold remobilization associated with Mississippi Valley-type fluids: A Pb isotope perspective. GSA Bulletin, 130, 1583–1595.

Hastie, E.C.G., Kontak, D.J., and Lafrance, B. (2020) Gold remobilization: Insights from gold deposits in the Archean Swayze Greenstone Belt, Abitibi Subprovince, Canada. Economic Geology, 115, 241–277.

Heinrich, C.A. (2007) Fluid-fluid interactions in magmatic-hydrothermal ore formation. Reviews in Mineralogy and Geochemistry, 65, 363–387.

Huang, B., Ni, P., Xiang, H.L., Wang, G.G., Yang, Y.L., Pan, J.Y., Li, S.N., and Bao, T. (2017) The Geological characteristics and ore genesis of the Qiucun gold deposit, Fujian Province. Bulletin of Mineralogy, Petrology and Geochemistry, 36, 650–658

(in Chinese with English abstract).
Jiang, Q.Y. (2015) Geological characteristics and prospecting significance of Dongyang gold deposit in Dehua County, Fujian Province. Geol. Fujian, 34, 27–32 (in Chinese with English abstract).
Jochum, K.P., Willbold, M., Raczek, I., Stoll, B., and Herwig, K. (2005) Chemical characterisation of the USGS reference glasses GSA-1G, GSC-1G, GSD-1G, BCR-2G, BHVO-2G and BIR-1G using EPMA, ID-TIMS, ID-ICP-MS and LA-ICP-MS. Geostandards and Geoanalytical Research, 29, 285–302.
Kerr, M.J., Hanley, J.J., Kontak, D.J., Morrison, G.G., Petrus, J., Fayek, M., and Zajacz, Z. (2018) Evidence of upgrading of gold tenor in an orogenic quartz-carbonate vein system by late magmatic-hydrothermal fluids at the Madrid Deposit, Hope Bay Greenstone Belt, Nunavut, Canada. Geochimica et Cosmochimica Acta, 241, 180–218.
Kouzmanov, K., and Pokrovski, G.S. (2012) Hydrothermal controls on metal distribution in Cu (-Au-Mo) porphyry systems. SEG Special Publication, 16, 573–618.
LaFlamme, C., Sugiono, D., Thebaud, N., Caruso, S., Fiorentini, M., Selvaraja, V., Jeon, H., Voute, F., and Martin, L. (2018) Multiple sulfur isotopes monitor fluid evolution in an orogenic gold deposit. Geochimica et Cosmochimica Acta, 222, 436–446.
Large, R.R., Danyushevsky, L., Hollit, C., Maslennikov, V., Meffre, S., Gilbert, S., Bull, S., Scott, R., Emsbo, P., Thomas, H., Singh, B., and Foster, J. (2009) Gold and trace element zonation in pyrite using a laser imaging technique: Implications for the timing of gold in orogenic and Carlin-style sediment-hosted deposits. Economic Geology, 104, 635–668.
Large, R.R., Bull, S.W., and Maslennikov, V.V. (2011) A carbonaceous sedimentary source-rock model for Carlin-type and orogenic gold deposits. Economic Geology, 106, 331–358.
Lawley, C.J.M., Jackson, S., Yang, Z., Davis, W., and Eglington, B. (2017) Tracing the transition of gold from source to sponge to sink. Economic Geology, 112, 169–183.
Li, S-N., Ni, P., Bao, T., Li, C-Z., Xiang, H-L., Wang, G-G., Huang, B., Chi, Z., Dai, B-Z., and Ding, J-Y. (2018a) Geology, fluid inclusion, and stable isotope systematics to the Dongyang epithermal gold deposit, Fujian Province, southeast China: Implications for ore genesis and mineral exploration. Journal of Geochemical Exploration, 195, 16–30.
Li, S-N., Ni, P., Bao, T., Xiang, H-L., Chi, Z., Wang, G-G., Huang, B., Ding, J-Y., and Dai, B-Z. (2018b) Genesis of the Ancun epithermal gold deposit, southeast China: Evidence from fluid inclusion and stable isotope data. Journal of Geochemical Exploration, 195, 157–177.
Li, X-H., Fan, H-R., Yang, K-F., Hollings, P., Liu, X., Hu, F.F., and Cai, Y-C. (2018) Pyrite textures and compositions from the Zhuangzi Au deposit, southeastern North China Craton: implication for ore-forming processes. Contributions to Mineralogy and Petrology, 173, 73.
Li, S-N., Ni, P., Wang, G-G., Bao, T., Huang, B., and Dai, B-Z. (2020) The Jurassic volcanic-intrusive complex in the Dehua gold orefield, coastal region of SE China: Implications for the tectonic setting and epithermal mineralization. Journal of Asian Earth Sciences, 197, 104390.
Liu, Q-S. (2018) Geological characters and ore-forming material sources of the Qiucun gold deposit. World Nonferrous Metal, 11, 85–86 (in Chinese with English abstract).
Liu, Y., Hu, Z., Gao, S., Günther, D., Xu, J., Gao, C., and Chen, H. (2008) In situ analysis of major and trace elements of anhydrous minerals by LA-ICP-MS without applying an internal standard. Chemical Geology, 257, 34–43.
Ma, Y., Jiang, S-Y., Frimmel, H.E., Xiong, S-F., Zhu, L-Y., and Chen, R-S. (2021a) Early Paleozoic orogenic gold deposit in the Cathaysia Block, China: A first example from the Shuangqishan deposit. Gondwana Research, 91, 231–253.
Ma, Y., Jiang, S-Y., Frimmel, H.E., Zhu, L-Y., Xiong, S-F., Chen, R-S., and Li, X-X. (2021b) Genesis of the Hebaoshan gold deposit in Fujian Province of Southeast China: Constraints from a combined fluid inclusion. H-O-C-S-Pb-He-Ar Isotope and Geochronological Study. https://doi.org/10.1007/s00126-021-01046-3.
Migdisov, A.A., Zezin, D., and Williams-Jones, A.E. (2011) An experimental study of cobalt (II) complexation in $Cl^-$ and $H_2S$-bearing hydrothermal solutions. Geochimica et Cosmochimica Acta, 75, 4065–4079.
Morey, A.A., Tomkins, A.G., Bierlein, F.P., Weinberg, R.F., and Davidson, G.J. (2008) Bimodal distribution of gold in pyrite and arsenopyrite: Examples from the Archean Boorara and Bardoc shear systems, Yilgarn craton, Western Australia. Economic Geology, 103, 599–614.
Ni, P., Pan, J.Y., Huang, B., Wang, G.G., Xiang, H.L., Yang, Y.L., Li, S.N., and Bao, T. (2018) Geology, ore-forming fluid and genesis of the Qiucun gold deposit: Implication for mineral exploration at Dehua prospecting region, SE China. Journal of Geochemical Exploration, 195, 3–15.
Ohmoto, H. (1972) Systematics of sulfur and carbon isotopes in hydrothermal ore deposits. Economic Geology, 67, 551–578.
Ohmoto, H., and Rye, R.O. (1979) Isotopes of sulfur and carbon. In H.L. Barnes, Ed., Geochemistry of Hydrothermal Ore Deposits. Wiley, 509–567.
Peterson, E., and Mavrogenes, J. (2014) Linking high-grade gold mineralization to earthquake-induced fault-valve processes in the Porgera gold deposit, Papua New Guinea. Geology, 42, 383–386.
Putnis, A. (2009) Mineral replacement reactions. Reviews in Mineralogy and Geochemistry, 70, 87–124.
Reich, M., Simon, A., Deditius, A., Barra, F., Chryssoulis, S., Lagas, G., Tardani, D., Knipping, J., Bilenker, L., Sánchez-Alfaro, P., Roberts, M.P., and Munizaga, R. (2016) Trace element signature of pyrite from the Los Colorados iron oxide-apatite (IOA) deposit, Chile: A missing link between Andean IOA and iron oxide copper-gold systems? Economic Geology, 111, 743–761.
Reich, M., Kesler, S.E., Utsunomiya, S., Palenik, C.S., Chryssoulis, S.L., and Ewing, R.C. (2005) Solubility of gold in arsenian pyrite. Geochimica et Cosmochimica Acta, 69, 2781–2796.
Shu, L., Wang, B., Cawood, P.A., Santosh, M., and Xu, Z. (2015) Early Paleozoic and Early Mesozoic intraplate tectonic and magmatic events in the Cathaysia Block, South China. Tectonics, 34, 1600–1621.
Simon, G., Kesler, S.E., and Chryssoulis, S. (1999) Geochemistry and textures of gold-bearing arsenian pyrite, Twin Creeks, Nevada: Implications for deposition of gold in Carlin-type deposits. Economic Geology, 94, 405–421.
Sung, Y.-H., Brugger, J., Ciobanu, C., Pring, A., Skinner, W., and Nugus, M. (2009) Invisible gold in arsenian pyrite and arsenopyrite from a multi-stage Archaean gold deposit: Sunrise dam, Eastern Goldfields province, Western Australia. Mineralium Deposita, 44, 765–791.
Sykora, S., Cook, D.R., Meffre, S., Stephanov, A.S., Gardner, K., Scott, R., Selley, D., and Harris, A.C. (2018) Evolution of pyrite trace element compositions from porphyry-style and epithermal conditions at the Lihir gold deposit: Implications for ore genesis and mineral processing. Economic Geology, 113, 193–208.
Velásquez, G., Beziat, D., Salvi, S., Siebenaller, L., Borisova, A.Y., Pokrovski, G.S., and De Parseval, P. (2014) Formation and deformation of pyrite and implications for gold mineralization in the El Callao District, Venezuela. Economic Geology, 109, 457–486.
Wang, J., and Li, Z.X. (2003) History of Neoproterozoic rift basins in South China: Implications for Rodinia break-up. Precambrian Research, 122, 141–158.
Wang, F.Y., Ge, C., Ning, S.Y., Nie, L.Q., Zhong, G.X., and Nole, C.W. (2017) A new approach to LA-ICP-MS mapping and application in geology. Acta Petrologica Sinica, 33, 3422–3436 (in Chinese with English abstract).
White, N.C., Zhang, D., Hong, H., Liu, L., Sun, W., and Zhang, M. (2019) Epithermal gold deposits of China: An overview. SEG Special Publication, 22, 235–262.
Williams-Jones, A.E., Bowell, R.J., and Migdisov, A.A. (2009) Gold in solution. Elements, 5, 281–287.
Wilson, S.A., Ridley, W.I., and Koenig, A.E. (2002) Development of sulfide calibration standards for the laser ablation inductively coupled plasma mass spectrometry technique. Journal of Analytical Atomic Spectrometry, 17, 406–409.
Wohlgemuth-Ueberwasser, C.C., and Jochum, K.P. (2015) Capability of fs-LA-ICP-MS for sulfide analysis in comparison to ns-LA-ICP-MS: reduction of laser induced matrix effects? Journal of Analytical Atomic Spectrometry, 30, 2469–2480.
Wu, F.Y., Lin, J.Q., Wild, S.A., Zhang, X.O., and Yang, J.H. (2005) Nature and significance of the Early Cretaceous giant igneous event in eastern China. Earth and Planetary Science Letters, 233, 103–119.
Wu, Y-F., Evans, K., Li, J-W., Fougerouse, D., Large, R.R., and Guagliardo, P. (2019) Metal remobilization and ore-fluid perturbation during episodic replacement of auriferous pyrite from an epizonal orogenic gold deposit. Geochimica et Cosmochimica Acta, 245, 98–117.
Zhang, H., Cai, Y., Zhang, Y., Ni, P., Li, S., Ding, J., Pan, Y., and Bao, T. (2018) Mineralogical characteristics of silver minerals from the Dongyang Gold deposit, China: Implications for the evolution of epithermal metallogenesis. Journal of Geochemical Exploration, 195, 143–156.
Zhai, D., Williams-Jones, A.E., Liu, J., Selby, D., Voudouris, P.C., Tombros, S., Li, K., Li, P., and Sun, H. (2020) The genesis of the giant Shuangjianzishan epithermal Ag-Pb-Zn deposit, Inner Mongolia, Northeastern China. Economic Geology, 115, 101–128.
Zhong, J., Pirajno, F., and Chen, Y.J. (2017) Epithermal deposits in South China: Geology, geochemistry, geochronology, and tectonic setting. Gondwana Research, 42, 193–219.
Zhou, X.M., Sun, T., Shen, W.Z., Shu, L.S., and Niu, Y.L. (2006) Petrogenesis of Mesozoic granitoids and volcanic rocks in South China: A response to tectonic evolution. Episodes, 29, 26–33.
Zhu, Z.Y., Cook, N.J., Yang, T., Ciobanu, C.L., Zhao, K.D., and Jiang, S.Y. (2016) Mapping of S isotopes and trace elements in sulfides by LA-(MC)-ICP-MS: potential analytical problems, improvements and implications. Minerals, 6, 110.

Manuscript received February 24, 2021
Manuscript accepted May 28, 2021
Manuscript handled by Matthew Steele-MacInnis

## Endnote:

[1]Deposit item AM-22-68030, Online Materials. Deposit items are free to all readers and found on the MSA website, via the specific issue's Table of Contents (go to http://www.minsocam.org/MSA/AmMin/TOC/2022/Jun2022_data/Jun2022_data.html).